Slaven Kalenjuk, BSc

Surface evaluation of large concrete dams with state-of-the-art total stations

MASTER'S THESIS

to achieve the university degree of

Diplom-Ingenieur

Master's degree programme: Geomatics Science

submitted to

Graz University of Technology

Supervisor

Univ.-Prof. Dipl.-Ing. Dr.techn. Werner Lienhart

Institute of Engineering Geodesy and Measurement Systems

Graz, December 2016

AFFIDAVIT

I declare that I have authored this thesis independently, that I have not used other than the declared sources/resources, and that I have explicitly indicated all material which has been quoted either literally or by content from the sources used. The text document uploaded to TUGRAZonline is identical to the present master‘s thesis.

Date

Signature

Abstract

The behaviour of large water dams is continously monitored with a sophisticated network of different geodetic and geotechnical sensors. An important aspect for dam safety is the concrete's state, which is assessed by visual inspections of operating staff and documented with photographs. In this master thesis, a new approach for surface documentation and evaluation of concrete dams, considering scan and image data from a state-of-the-art total station, is presented. Based on practical measurements performed at the Hierzmann dam, a procedure for deriving a continous surface model is introduced. As it is shown, the dam's geometry is reproduced with millimeter accuracy and photo textures are aligned at subpixel level. Additionally, a new concept for long-term monitoring of a dam's surface is proposed, aiming to provide the basis for an objective assessment of the concrete's state. The potential of image processing techniques for automatic real-time on-site detection of defects as well as for identifying and quantifying surface changes is demonstrated by means of practical investigations.

Kurzfassung

Das Verhalten von großen Talsperren wird kontinuierlich mit einer Vielzahl an unterschiedlichen geodätischen und geotechnischen Sensoren überwacht. Ein entscheidender Faktor für die Standsicherheit ist die Betonqualität, die durch visuelle Inspektionen bewertet und mit Fotoaufnahmen dokumentiert wird. In dieser Masterarbeit wird eine Methode zur Oberflächendokumentation von Talsperren mit Scan- und Bilddaten einer modernen Totalstation vorgeschlagen. Am Beispiel der Sperre Hierzmann wird gezeigt, dass für das abgeleitete Oberflächenmodell eine geometrische Genauigkeit von wenigen Millimetern und eine Übereinstimmung der Bildtexturen im Subpixel-Bereich erzielbar ist. Außerdem wird ein neu entwickeltes Systemkonzept zur Langzeitüberwachung der Maueroberfläche vorgestellt, welches eine objektive Beurteilung des Betonzustandes ermöglichen soll. Anhand von praktischen Untersuchungen wird das Potenzial von Bildverarbeitungsalgorithmen zur automatischen und echtzeitfähigen Detektion von Schadstellen sowie zur Erfassung und Quantifizierung derer Veränderungen demonstriert.

Acknowledgements

I would like to thank my supervisor Univ.-Prof. Dipl.-Ing. Dr.techn. Werner Lienhart for his faith in me and for giving me the opportunity to work on this captivating topic. The enthusiasm he has shown for my thesis was inspiring and contagious. His invaluable comments and thoughtful advises have been a great help in developing new ideas and completing this work.

I am grateful to all members of the Institute of Engineering Geodesy and Measurement Systems contributing to this thesis. In particular, I want to thank Matthias Ehrhart for the insightful discussions about the functional principle of Image-Assisted Total Stations.

This thesis would not have been possible without Dipl.-Ing. Harald Wackenreuther. It was him who initiated a cooperation between Verbund Hydro Power GmbH and the institute. I have greatly benefited from talking to someone with so many years of experience in dam engineering. I want to thank him for all the provided support. Special thanks also to all colleagues in the surveying division in Kaprun for assisting me in practical measurements at the Drossen dam in Salzburg.

I want to express my deep thanks to my esteemed fellow student Žan Gojčič for all the support throughout the last year. Due to the countless discussions we had, I gained inestimable insights and motivation. He gave me constructive help in theoretical problems and assisted me in numerous practical measurements.

I am indebt to my friend Golo Wimmer, who offered me to proofread this thesis. Thank you!

At this point, I would like to express my gratitude to Christina Ehrhart for the continous encouragement, all given advices and the patience she has shown in the past years. Without her, I would not be where I am today.

Above all, I wish to thank my parents for their everlasting love and moral support in my life. I would like to aknowledge the large sacrifices they have made to ensure that I enjoyed the best possible education.

Contents

Abbreviations

CAD Computer-Aided Design

CLAHE Contrast Limited Adaptive Histogram Equalization

DBSCAN Density-Based Spatial Clustering of Applications with Noise

ECC Enhanced Correlation Coefficient

EDM Electronic Distance Measurement

FOV Field of View

GUI Graphical User Interface

HR High Resolution

IATS Image Assisted Total Station

ICOLD International Commission on Large Dams

IGMS Institute of Engineering Geodesy and Measurement Systems

MBR Minimum Bounding Rectangle

OAC On-Axis Camera

OpenCV Open Source Computer Vision

OVC Overview Camera

PPA Principle Point of Autocollimation

RGB Red-Green-Blue

SHM Structural Health Monitoring

SIFT Scale-Invariant Feature Transform

SLR Single-Lens Reflex camera

SNR Signal-to-Noise Ratio

TLS Terrestrial Laser Scanning

WFD Wave Form Digitizing

1 Introduction

1.1 Motivation

Hydropower has proven to be a reliable, cost-efficient and carbon-neutral technology for generating sustainable energy. By the end of 2015, more than 16% of the world's electricity generation was provided by water power plants (Regan, 2010). According to the International Energy Agency, the share of hydropower could be doubled by 2050 by primarily realising large new projects in emerging countries, as well as redeveloping existing water plants in industrialised countries.

An improvement to hydropower efficiency has been found through retaining water with different types of dams, which deliver economic, as much as environmental and social benefits. However, they pose potential threat to environment, property and person, as seen at the catastrophic failure of the Teton dam in 1976 at its first fill, resulting in death of eleven people and in large economic losses. Although a high percentage of incidents associated with dams occur in the first six years after construction (Regan, 2010), some failure modes become more likely with age, as dams are exposed to particular stresses over time, e.g. gravitational forces, water pressure and changing atmospheric conditions. Hence, a life-long surveillance of the dam's condition and behaviour is crucial to recognise anomalies, take timely action and consequently reduce the risk of a dam failure.

Dam surveillance is a major challenge, which is met by the International Commission on Large Dams (ICOLD), whose members are essentially practising engineers, geologists, scientists, consulting firms and construction companies. Appropriate guidelines were proposed in ICOLD (2013), in which the importance of automated monitoring solutions of significant parameters of the dam's behaviour is emphasised. Nevertheless, for the overall assessment of the dam safety, the visual on-site inspection of the dam and its surroundings, performed by the operational staff, remains irreplaceable.

1.2 Visual inspections of water dams

Visual inspections constitute a necessary component for identification of anomalies in the structural condition and behaviour of a dam. Appearance of cracks on a concrete wall indicates force influences, which may affect the stability of the structure. For that reason, construction work on the Ratwyl tunnel had to be stopped in 1979, when geodetic measurements revealed unexpected deformations and visual changes were spotted in terms of cracks on the downstream and upstream face of the Tseuzier dam (Biedermann, 1980).

Within the scope of visual inspections, examinations are carried out to identify relevant changes on the structure and its surroundings, where special emphasis is put on the

detection and monitoring of well-known deficiencies of water dams. Weaknesses and their location in the case of concrete walls are given in Table 1-1. In particular, regular dam inspections to detect concrete problems such as disintegration, scaling, cracking, efflorescence, erosion, spalling and popouts, are essential, as explained in Ohio Department of Natural Resources (1999).

Table 1-1: Scope of visual inspections for concrete dams (ICOLD, 2013)

Part of dam	**Defect of interest**	
Downstream face	surface seepage water	sinter formation
	cracks, joint openings	condition of concrete/masonry
	ice formation	
Dam crest	cracks	joint movements
Upstream face	Vortex formation	condition of concrete/masonry
	cracks, joint openings	
Inspection gallery, shafts and adits	leakage seepage water	sinter formation
	cracks, joint movement	condition of concrete/masonry
	line of sight-check	clogging of drainage system

Visual inspections aim to monitor the deterioration process over time. Therefore, size, shape and state of the above mentioned defects are recorded and submitted to public authorities every few years. Nowadays, annotations, drawings and photos are commonly used to depict the current situation. Regarding the image takings, currently a standard Single-Lens Reflex camera (SLR) is used to acquire photos of regions of interest from several shooting locations, which are referenced in a Computer-Aided Design (CAD) blueprint of the concrete wall (cf. Chapter C, Verbund 2011, p. 3).

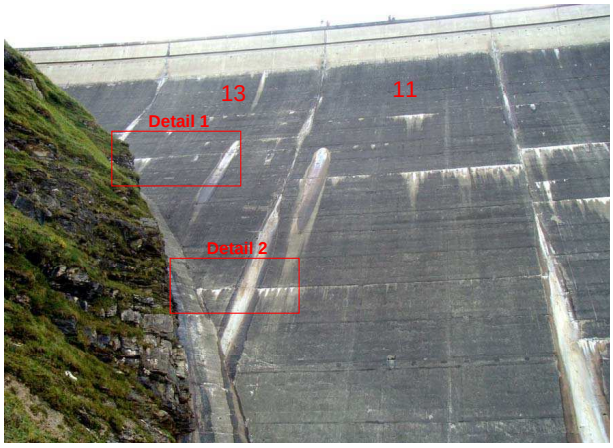

Figure 1-1: Example of surface documentation of a water dam, Verbund (2011, p. 8)

From the perspective of dam operators, the current methodology for surface documentation has proved insufficiencies with respect to the following aspects:

Access to region of interest is required. Images captured at small angles of incidence and great distances, as e.g. depicted in Figure 1-1, provide only a coarse documentation. Therefore, new approaches were considered for realising orthogonal close-shots across the whole downstream side, by e.g. elaborately operating a suspended platform with a remote-triggered camera from the dam crest (senseFly, 2016).

Metric information, for instance, about defects, comprising length, width of cracks, cannot be derived from the above-described method. It has been noted, however, that these parameters constitute valuable data for assessment of the concrete state.

Detection of visual changes of the dam's surface is considered to be improbable from photos as displayed above. However, there is a need for identification of long-periodic deterioration processes, i.e. changes which are not recognisable by daily inspections by operating staff. Experience with the Koelnbrein dam has shown that concrete stabilisation by injections has to take place in time to prevent further dam degradation and potential failure (Regan, 2010).

1.3 Proposed new method for surface evaluation of concrete dams

The goal of the present thesis is to find solutions for improving surface documentation and evaluation of large water dams. A new surface monitoring concept is introduced as a supplement to existing Structural Health Monitoring (SHM) solutions of water dams. The system, consisting of a state-of-the-art total station and a laptop, is characterised by the following key features:

- Automatic in-situ identification and registration of defects
- Change detection of surface conditions
- Quantification of prominent features, dimensions and changes of regions of interest
- (Semi-) Automatic operation for permanent or selective use
- Good basis for closer visual examinations by civil engineers

A more precise description about the developed concept is provided in Chapter 2. The workflow for mapping the water dam's surface with a state-of-the-art total station is presented in Chapter 3. Based on practical measurements, possible outcomes and their achievable accuracy are demonstrated. The underlying idea and an approach for automatic

detection of defects and their high-resolution acquisition are introduced in Chapter 4. Then, different techniques for automatic change detection and quantification of a concrete dam's surface condition are outlined in Chapter 5. Finally, a comparison of the traditional approach for documenting a dam's surface and the new proposed one is given in Chapter 6.

1.4 Instrumentation and scope conditions

The system's main components are an Image Assisted Total Station (IATS) with scanning functionality, a standard laptop computer and a connection cable (cf. Table 1-2 for detailed information). Algorithms for special data acquisition and for data processing were developed in Python programming language in combination with open-source libraries, e.g. Open Source Computer Vision (OpenCV).

Table 1-2: Information about the instrumentation used in this thesis

IATS	Instrument	Leica MS60 I R2000
	Serial number	882001
	On-board SW version	Captivate 2.00
	Remote control	GeoCOM protocol over TCP/IP
	Connection cable	Leica GEV234
Laptop	Model	HP ProBook 4420s
	Operating system	Windows 7 64-Bit
	Hardware specifications	Intel Core i3, 4 GB RAM
	Python version	2.7
	OpenCV version	3.0.0

Results detailed in this thesis are based on investigations conducted under different circumstances and different locations. System prototyping was performed at the Institute of Engineering Geodesy and Measurement Systems (IGMS), practical experiments were carried out at the Austrian concrete arch dams Hierzmann in Edelschrott, Styria and Drossen in Kaprun, Salzburg.

2 Surface monitoring of water dams with a state-of-the-art total station

The main challenge for a surface monitoring solution is to provide valuable information for assessing a dam's concrete state. This chapter shows how the newly proposed method attempts to meet this challenge and how the basic operating principle is designed.

2.1 Importance for dam safety assessment

Figure 2-1 schematically illustrates the developed monitoring solution and its major modules, displayed as blue boxes. In combination with the data from an IATS, the key objectives, namely surface documentation and evaluation, can be achieved. As an output, a snapshot of the current situation is delivered with detailed and geo-referenced recordings of defects. Furthermore, metric information is provided, so that measurements on the concrete wall are enabled without direct access. Including the information from previous documentations, changes are identified and quantified.

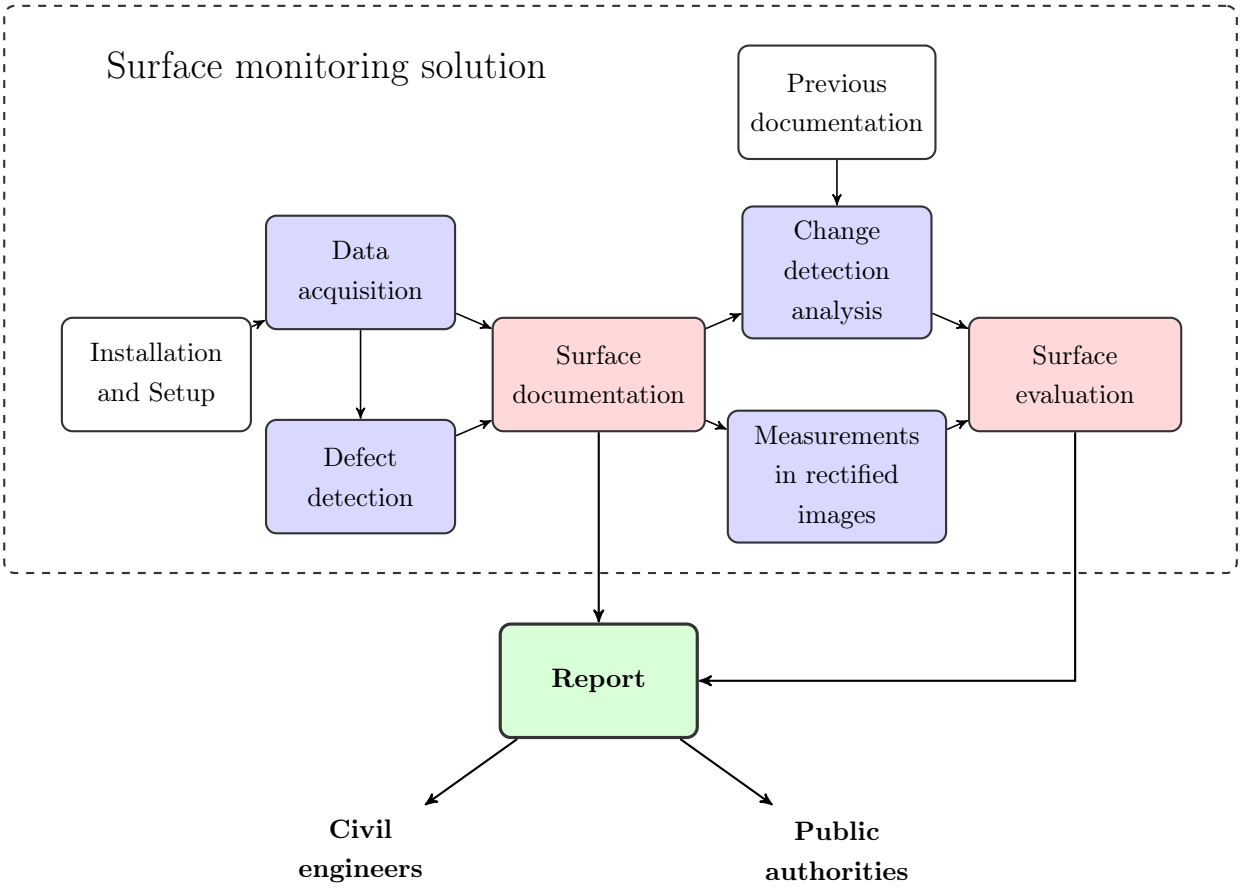

Figure 2-1: Surface monitoring solution as key component in the assessment of the concrete's state

As a large number of other different sensors are installed for monitoring the dam's behaviour, the proposed solution has to be understood as a supplement and not as a replacement of existing monitoring approaches.

Concrete degradation is a long-term process, thus, the system is intended for selective, not for permanent use. However, continuous monitoring may be required for a short period in case that water dams become subject to new or additional stresses, such as construction works, natural risks or introduction of a pumped-storage operation. Additional value of a fixed and permanent installation of the system is provided in case when checks are not performed regularly by operating staff, as e.g. in some cases in the U.S. (DePalma, 2008).

2.2 Functional principle

A schematic representation of the functional principle of the developed surface monitoring solution is depicted in Figure 2-2.

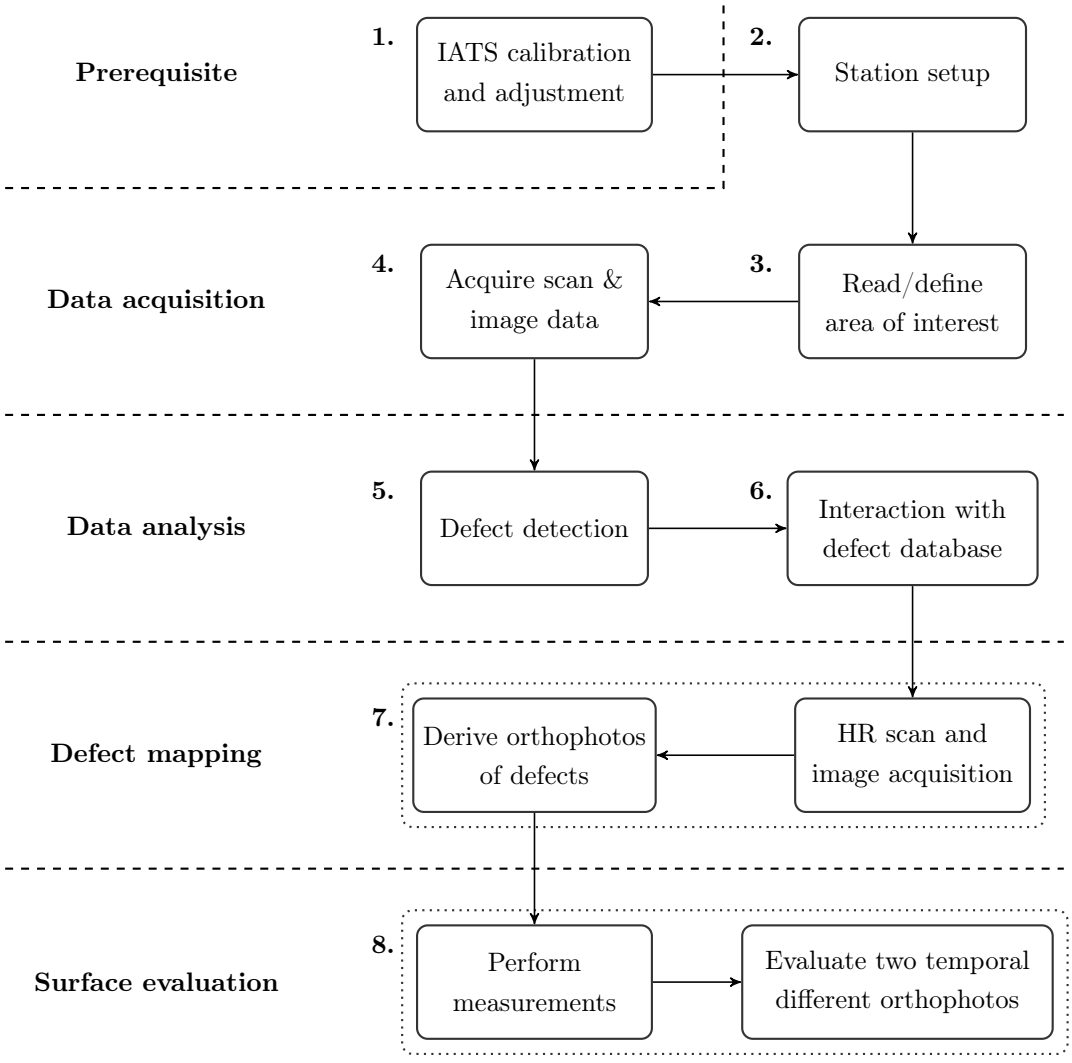

Figure 2-2: Functional principle of proposed surface monitoring solution with an IATS

1. IATS calibration and adjustment:
   The fundamental idea of the developed new concept is the combination of different data types, i.e. angles, distances and images, which is why an instrument calibration is required. Apart from the well-known corrections for axis errors, the projection centre offset w.r.t. the theodolite centre and the camera tilt w.r.t. the telescope orientation have to be taken into account. Interior and exterior orientation parameters for the cameras of the Leica MS60 Multi Station are discussed in Chapter 3.4.2. Moreover, systematic error sources affecting the distance measurement, e.g. meteorology, need consideration as well.

2. Station setup:
   The instrument has to be set up in a local 3D or a national 2.5D (map projection) reference system. This procedure ensures a correct linkage of all measurements from different setup points and from different epochs. Hence, fixed points with known coordinates are preconditioned.

3. Definition of surface region of interest:
   The outline of the surface region for documentation is specified by selectively measuring points on the dam. The coordinates are saved for computing orientation angles from every observation point, i.e. from temporarily or locally different points. Using the camera orientation parameters, the point coordinates are converted from object into image space. As a consequence, image analysis is confined to the polygon, which is shaped by these points.

4. Scan and image data acquisition:
   The concrete surface is sampled with equidistant turning angles within the border lines with a scanning resolution based on the surface's structure. The texture is captured by photos of the IATS wide-angle camera and furthermore orientation parameters are stored for each image. Merging scan and image data, referred to as surface mapping throughout this thesis, opens up new possibilities by yielding novel products, such as 3D photo-models and orthophotos of a water dam. The process of surface mapping with data from an IATS, is explained in detail in Chapter 3.

5. Automatic defect detection:
   Images, acquired in the previous step, are downloaded to the laptop and analysed on possible defects. According to Table 1-1, any irregularities on the concrete surface could pose a potential defect, which is exactly what is being exploited for defect detection (cf. Chapter 4). The Minimum Bounding Rectangle (MBR) of the detection, expressed in terms of horizontal (Hz) and vertical (V) angles, is computed.

6. Interaction with defect database:
   Coordinates of detected MBRs from previous surveys are read in from the database and transformed into image space. These serve as additional information for filtering mistakenly or insufficiently detected defects. Algorithms described in Chapter 4 are applied to extract the MBRs of interest, i.e. which are presumed defects.

7. Defect mapping:
   Defects, which are automatically detected by the system at site, are captured with High Resolution (HR), i.e. point clouds with a higher sampling rate and photos with high optical magnification are gathered. For defect mapping, a surface mapping based on HR data of the defects is used. Individual orthophotos are derived from 3D photo-models of all defects.

8. Evaluate surface conditions:
   In fact, orthophotos constitute a key feature of the proposed monitoring solution. Metric information is provided and measurements on the concrete surface can be performed without direct access. Identification of changes is at least as important as the documentation of the current situation. Therefore, different change detection algorithms have been refined and tested on two orthophotos of the same defect, based on data from different times. Methods for identifying changes and their extent on a concrete wall are outlined in Chapter 5.

3 Surface mapping with scan and image data

Previous studies on surface mapping have shown that there exists a potential of merging geometry and optical information for documenting the dam's surface condition. In senseFly (2016), results of mapping the downstream face of the Tseuzier dam by using an inspection drone, equipped with a high resolution camera, is presented. Overlapping images are processed using photogrammetry and computer vision tools to obtain 3D point clouds, textured models and orthophotos. However, this approach is rather sophisticated and time-consuming, as 6.5 flying days, 7000 photos and two weeks of processing were required to get a full coverage of the Tseuzier dam with a spatial resolution of 0.6 mm.

An alternative approach with less computational cost was proposed e.g. in Camp et al. (2013). A system for defect mapping of concrete and metal materials is introduced, whose functional principle is demonstrated for a concrete dam. The system consists of a 3D laser scanner and a high resolution camera with a 600 mm telephoto lens. Nonetheless, the exact fusing of data from different observation points and from both instruments poses a key challenge to this system.

A state-of-the-art IATS with scanning functionality delivers both types of data and therefore provides additional benefits:

- Referring photos and scan data to one reference system is easy, as the offset from camera to telescope centre is calibrated during production. Thus, exterior camera parameters and orientation is known for each image.
- Relative alignment of scans from different observation points is given by the station setup. The correct position and orientation of the point cloud is determined before acquisition via e.g. resection, and thus there is no need for time-consuming post-processing procedures.
- Meteorological corrections are directly applied to the sampled points as well, analogously to individual distances, measured by a standard total station.

The basic workflow for surface mapping with scan and image data is illustrated in Figure 3-1. Note that Terrestrial Laser Scanning (TLS) and imaging are considered separately due to different processing techniques, albeit realised by one instrument. After data acquisition, point clouds from different observation points are merged and points sampled from other objects but the concrete wall are removed. Next, a continuous surface model is extracted from scan data with algorithms described in Chapter 3.1. Image processing techniques might be necessary to compensate colour differences between different photos before mapping them onto the surface model. This process is commonly called

texture mapping, as the oriented images, which are used for mapping, are called textures (cf. Chapter 3.2). As a result, a textured 3D model of the water dam's surface, also referred to as 3D photo-model, is obtained. Finally, the surface model, which combines geometry and image data, is mapped orthographically onto an image plane to generate a raster image with correct referencing and metric information (cf. Chapter 3.3).

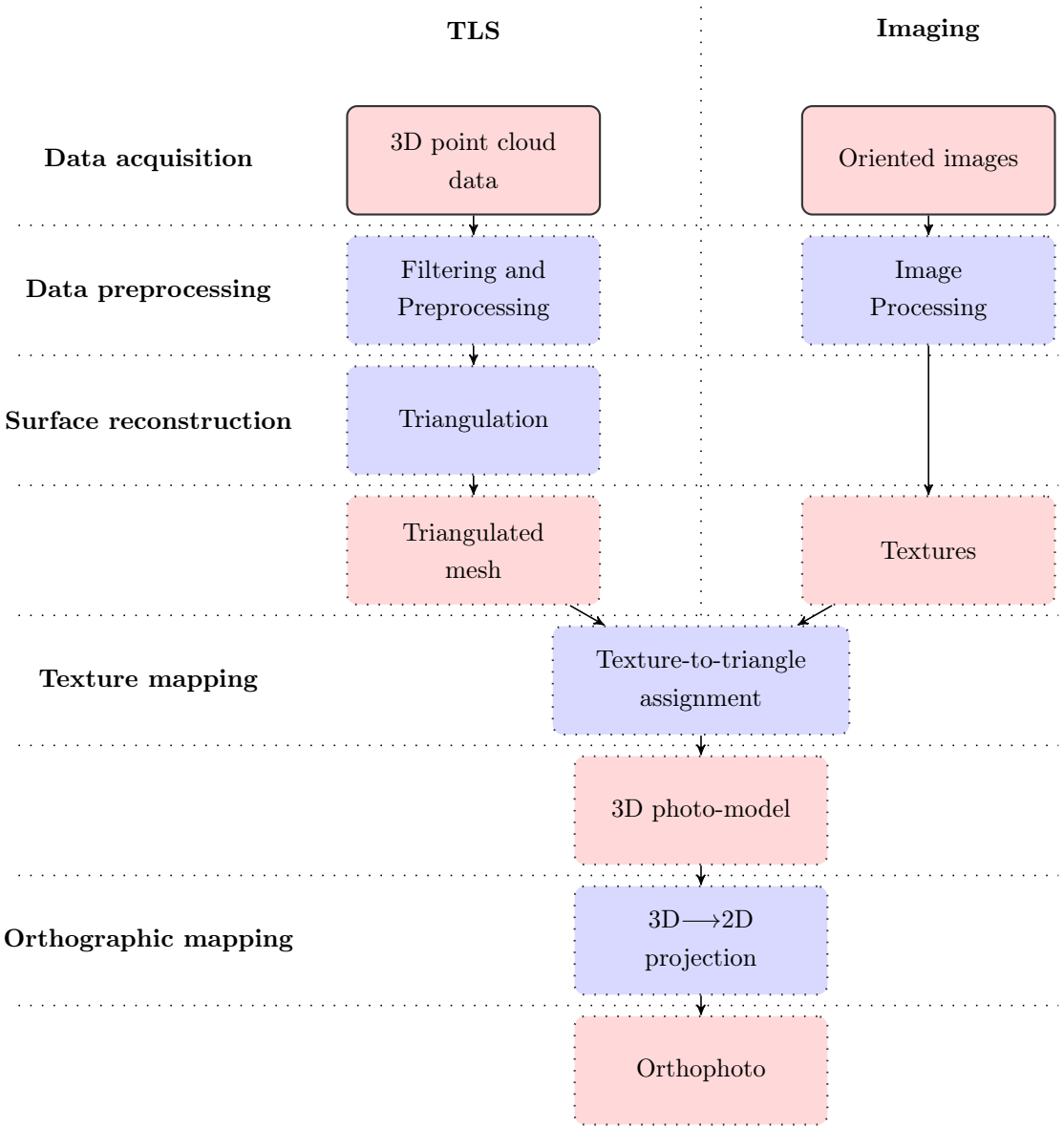

Figure 3-1: Proposed workflow for surface mapping with scan and image data

Figure 3-2 visualises exemplary results of the aforementioned methodology for surface mapping of a concrete dam with an IATS. The achievable quality of the proposed workflow using an IATS is evaluated in Chapter 3.4.

(a) Scan data classified by RGB values

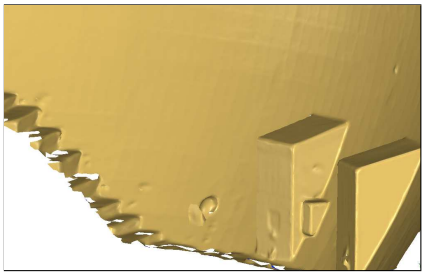

(b) Triangulated mesh

(c) Textured digital surface model

(d) Orthophoto of mapped defect (red rectangle) of a concrete dam, 2mm/px

Figure 3-2: Example for surface mapping of a concrete arch dam with an IATS

3.1 Surface reconstruction from point cloud data

TLS is a well-developed technology to acquire 3D geometry of natural and man-made objects. The supplied point cloud provides a discretisation of the object's surface and serves for analysis and visualisation. The quality of the representation depends to a large extent on the sampling density and on the object's structure. In case of TLS, angular resolution and object distance to the instrument narrow the achievable point cloud density. Also, from an economical point of view, an infinitesimal point spacing is not worth the high expenditure of time.

Therefore, it has been proposed to depict the object's characteristics by reconstructing a continuous surface model from a limited point number (e.g. acquired by TLS). Starting from appropriate research on this idea from the 1980's (cf. Boissonnat (1984)), the digital representation of real world objects has become a longstanding objective in the field of computer graphics. Today, various disciplines make use of continuous digital models for surface-oriented visualisation (e.g. medicine, cellular biology, material science, engineering, mapping and cartography).

Hoppe et al. (1992, p. 19) formulates the problem of surface reconstruction more precisely as follows: A set $P = \{p_1, p_2, \ldots, p_n \mid p_i \in \mathbb{R}^3\}$ of points sampled from a surface S provides the basis for an approximation of S. The points can be written as $p_i = s_i + e_i$,

for $s_i \in S$ and randomly distributed errors e_i accounting for imperfect measurements.

In consideration of surface recovering from scattered point cloud data, the following steps are required from a practical point of view:

1. Pre-processing of point cloud data:
   As outlined above, the sampled points need to be scattered around the real surface. In this step, scans from different setups are fused, outliers are eliminated and break lines are defined to keep the edges. The influence of potential imperfections in the point cloud data on the surface determination process is discussed in Section 3.1.2

2. Generation of a digital, continuous representation of the surface:
   Based upon the characteristics of the available point cloud data, different methods for surface reconstruction exist. In order to get an idea on what to pay attention to and what to expect, a rough overview on different approaches and their theory is given in Section 3.1.1.

3. Post-processing of the digital surface model:
   Correction operations of the digital model may be necessary, and this depends mostly on the input data's quality. Above all, such corrections include refinement operations for extracting more details and gap filling to obtain a watertight model, which constitutes a product required in many disciplines. For more details on post-processing surface data, the reader is referred to Weyrich et al. (2004).

3.1.1 Overview of different surface reconstruction approaches

As stated in Cazals and Giesen (2004), a requirement for the reconstruction process is that the digital model matches the original in terms of geometric and topological properties. Meeting these conditions is challenging, because surface reconstruction generally states an ill-posed problem, as there are an infinite number of surfaces, which may pass through or near the data points (see definition of reconstruction problem above).

Hence, a lot of algorithms are based on assumptions imposed on point cloud data and the object's shape. In particular, information about sampling density, level of noise and scanning direction provide valuable input for the reconstruction process. Knowledge on the scanned shape, e.g. local surface smoothness, presence of boundaries and edges, symmetries and regularities, is also important (Berger et al., 2014).

The appropriate reconstruction algorithm for a specific case is defined by characteristics of input data and the choice of how the final outcome should look like. The digital surface may be represented in many different ways. Therefore, the wide range of surface reconstruction methods is classified by the type of representation. An overview of the three most important approaches is presented below.

Simplicial representation

One approximation method makes use of simplicies, i.e. triangles in $\mathbb{R}^2$ and tetrahedra in $\mathbb{R}^3$ (see Figure 3-3a). For that reason, surface reconstruction is often associated with triangulation and the resulting surface model is referred to a triangulated mesh. In Gomes et al. (2009) two categories of triangulation algorithms are stated: the well-known Delaunay-based ones (cf. Figure 3-3b), and algorithms based on region-growing-techniques.

The latter is a simpler surface reconstruction class, which, however, is not as robust against unorganised points, i.e. when no additional information about the point cloud data is given. Even though there exist hybrid forms exploiting benefits of both approaches (cf. Kuo and Yau (2005)), Delaunay-based methods are more commonly used.

The special features of the Delaunay triangulation are its uniqueness and its property of minimising the radius of the circumscribing sphere of the simplicies. As a consequence, the minimum angle is maximised and hence well-shaped simplicies are provided.

In practice, one simple approach for realising a Delaunay triangulation is to assume a coordinate system where every (x, y) coordinate is assigned to only one z value. Thereby the problem is reduced to $\mathbb{R}^{2.5}$ and thus all points are mapped to the x, y plane and the Delaunay and Voronoi diagram is built up in two dimensional space (cf. Figure 3-3b).

In three-dimensional space the issue is much more complex, where the Delaunay triangulation is established by partitioning the convex hull of the sample points into small adjacent tetrahedra, where the circumscribing sphere of each simplex must not contain any other data points (cf. Bajaj et al. (1995)). The difficulty is to find those simplicies which actually belong to the surface. The triangulated surface extraction is explained in more detail in Gomes et al. (2009) and Maur (2002).

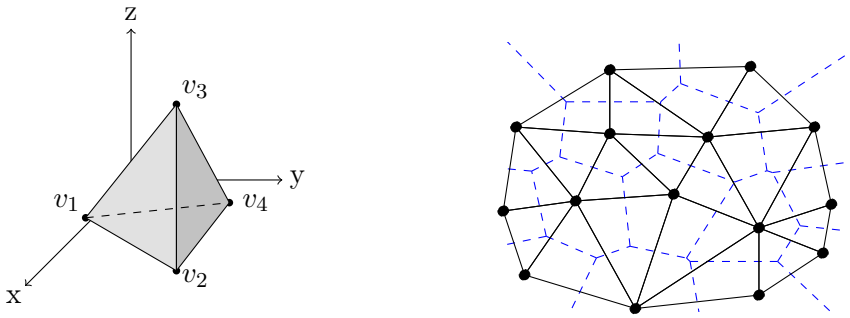

(a) Tetrahedron as simplex in three-dimensional space

(b) Duality of Delaunay and Voronoi graph

Figure 3-3: Illustration of simplicial surface representation in $\mathbb{R}^2$ and $\mathbb{R}^3$

Parametric representation

The aim is to find a surface S, which can be defined by a function $F(u, v)$, passing through or approximating the point cloud. According to Gomes et al. (2009), the procedure consists of four main steps: First, a mesh is generated using e.g. the marching-cubes algorithm, 3D Delaunay triangulation and α-shapes. The mesh is consequently partitioned into small patches, which are individually parametrised, i.e. the functional parameters (u_i,v_i) are assigned to the points (x_i, y_i, z_i). When parametrising the patches separately, it is important to retain the local smoothness of the surface. Eventually, the surface fitting problem is solved by minimising the deviations from the data points using the least squares approach (Gomes et al., 2009, p. 229)

$$\sum_i ||x_i - F(u_i, v_i)||^2 \stackrel{!}{=} \min . \tag{3-1}$$

For F, Bézier curves and B-splines are usually chosen (Remondino, 2003, p. 3).

Implicit representation

Regarding surface fitting, it should be noted that implicit curves are suitable as well. An implicit representation is given by $F(\mathbf{x}) = 0$, where $\mathbf{x}$ denotes a point which lies on the surface if the function evaluates to zero. The obvious approach is to fit a single polynomial to the entire point cloud (Gotsman and Keren, 1998). Hoppe et al. (1992) had the idea to estimate a local signed distance function, which indicates the distance of a local tangent plane to the closest point. Positive distances are assigned to points located outside of the object and negative distances to points in the inside. Consequently, the zero set of the function consists of all points belonging to the surface, which is eventually reconstructed by simplicies. Other implicit representations have been developed, e.g. moving least squares methods (MLS, cf. Cheng et al. (2008)) and interpolation techniques using radial basis functions (RBF, cf. Carr et al. (2001)).

Another important method in this category is the Poisson surface reconstruction technique, which is e.g. used in the open-source project CloudCompare (2016). Apart from the data points, a vector field $\vec{V}$ of surface normals (cf. Figure 3-4a) is additionally required in each point to derive an indicator function χ_M. As defined by Kazhdan et al. (2006), this function assumes two cases

$$\chi_M(\mathbf{x}) = \begin{cases} 1 & \text{if } \mathbf{x} \in M \\ 0 & \text{if } \mathbf{x} \notin M \end{cases} . \tag{3-2}$$

The function evaluates to one, if the data point is inside of the model M (cf. Figure 3-4c)

and zero otherwise. Note that an enclosed surface S, here denoted as a model M, is retrieved (cf. Figure 3-6b).

The gradient vector field of this function is zero everywhere, except at those points close to the surface. The central idea is that the known surface normals should correspond to the evaluated gradient field at the data points (cf. Figure 3-4b). Hence, the task is to find the scalar field of the indicator function χ_M, whose gradient field $\nabla\chi_m$ fits best to the surface normals $\vec{V}$. This amounts to solving the Poisson equation

$$\Delta\chi_m = \nabla\vec{V} \; . \tag{3-3}$$

For details on solving the Poisson equation, the reader is referred to Kazhdan et al. (2006).

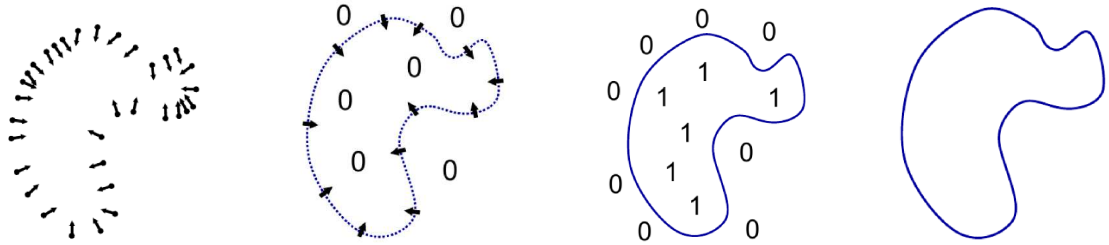

(a) Oriented point cloud $\vec{V}$ (b) Gradient of indicator function (c) Indicator function (d) Reconstructed model M

Figure 3-4: Illustration of the Poisson surface reconstruction in $\mathbb{R}^2$ (Kazhdan et al., 2006, Fig. 1)

Having computed the indicator function χ_M, the surface S is obtained by extracting an isosurface of the scalar field. As explained in Kazhdan et al. (2006), an accurate representation of the indicator function is necessary near the surface only, hence an adaptive octree subdivision with varying octree-depth (according to the surface's structure) is applied (cf. Figure 3-5). Using the marching-cubes algorithm, the data space is partitioned into small voxels (i.e. grid cells). Each voxel is analysed on whether it is passed through by the isosurface and if so, intersection points on edges of voxel cells are eventually taken for the generation of a triangulated mesh.

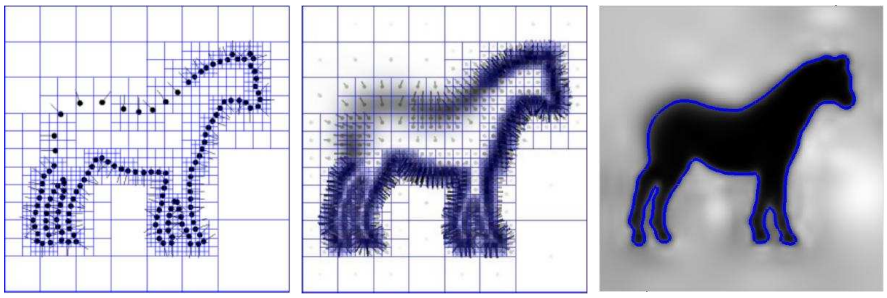

Figure 3-5: Example of isosurface extraction with octree subdivision in $\mathbb{R}^2$, (Gotsman and Kazhdan, 2008, pp. 11-15)

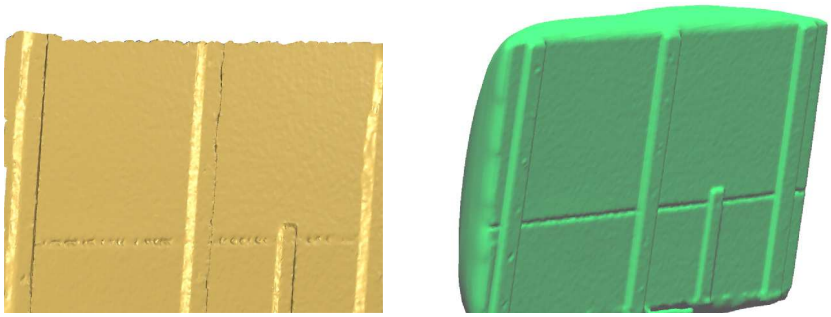

(a) Reconstructed surface model based on Delaunay triangulation, obtained in 3DReshaper (2016)

(b) Surface reconstruction with Poisson yields an enclosed model in CloudCompare (2016)

Figure 3-6: Exemplary results of surface reconstruction with two meshing algorithms

3.1.2 Challenges of surface reconstruction from scan data

The success of surface reconstruction is subject to the quality of sampling (i.e. scanning quality). Point cloud imperfections, which typically occur and influence the digital model, are depicted in Figure 3-7.

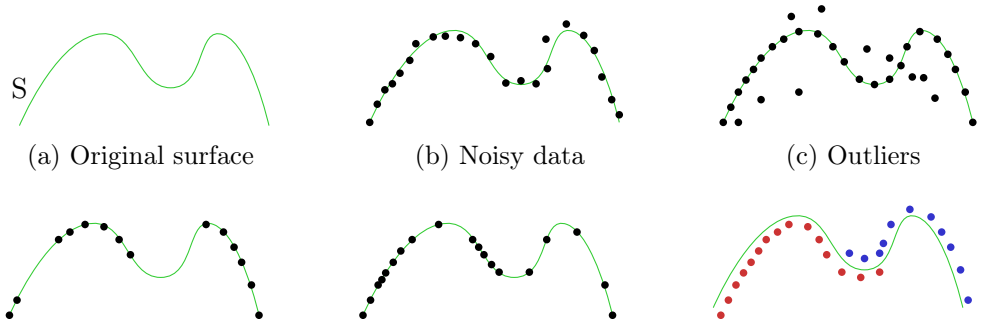

(a) Original surface

(b) Noisy data

(c) Outliers

(d) Missing points

(e) Non-uniform sampling density

(f) Misaligned scans

Figure 3-7: Different types of point cloud artefacts, illustrated for the 2D case, based on Berger et al. (2014)

Data noise is present in every observation and is considered as randomly distributed errors. Interpolation techniques, like the Delaunay triangulation, use original data points, which often yield jagged surfaces in case of noisy data. A solution to this problem is provided by computing an approximation of new points. The meshing algorithm in 3DReshaper (2016) for instance (cf. Figure 3-6a), partitions the data space into voxels, whose size is defined by the scanning resolution. For each voxel cell, the mean coordinate of all inlying points is computed and consequently used for triangulation. However, noise in point cloud data cannot be removed completely and should thus be evaluated for each object separately by computing the deviations from a fitted surface or mesh.

Outliers represent points, which differ significantly from the true surface. The causes for outliers are manifold and may be traced back to obstructions in the Field of View (FOV), surface or multipath reflections (Sotoodeh, 2007). They require either robust algorithms, i.e. ones which are able to handle such special data points (Mullen et al., 2010), or detecion and elimination procedures applied in advance (Lipman et al., 2007).

Missing points are a product of high light absorption, obstacles in the field of view and scan range limitations (Berger et al., 2014). Depending on the reconstruction algorithm, they either lead to holes in the surface (e.g. in the approach of 3DReshaper (2016)) or to very coarse approximations of the shape. The extent of missing data affects surfaces in different manners, according to their degree of detail.

Non-uniform sampling density results from scanning orientation, object-to-instrument distance as well as the geometric shape of the object. The knowledge of sampling density is vital for the reconstruction process, especially for *spatial subdivision* algorithms (cf. Mencl and Müller (1997)), as used e.g. in 3DReshaper (2016), where a uniform size of grid cells needs to be determined.

Misaligned scans imply false registration of point cloud data from different points of observation. For the case of two misregistered scans, statistical analysis of data-to-fitted surface (or mesh) deviations reveals a non-normal distribution but increased probability at two different spots (usually at deviations with opposite sign). However, registration through transformation might be expedient in post-processing.

3.2 Texture mapping

The importance of visual inspections for the assessment of dam safety has been already emphasised in Chapter 1.2. Information about the surface condition of a concrete dam cannot be derived from geometry only, i.e. from a triangulated mesh, since knowledge on texture content is equally required. Hence, the combination of geometry and texture is the major goal in order to provide a photo-realistic 3D model, which is assumed to yield benefits from either side and to open up new opportunities as well.

Texture mapping describes the process of mapping a 2D array (digital image) onto a surface model (e.g. triangulated mesh), obtained from e.g. techniques as outlined in Chapter 3.1.1. In the field of computer graphics, this is commonly accomplished by using texture maps. Roughly speaking, a texture map is a digital image referenced in a coordinate system with normalised texture coordinates $0 \leq (u, v) \geq 1$. The actual mapping process is provided through a functional relation between the texture map and mesh,

which is simply established by e.g. assigning texture coordinates to the mesh vertices (see Figure 3-8). For more information on texture mapping using such maps, the reader is referred to Hughes et al. (2013, pp. 547-567).

Figure 3-8: Example of a simple texture mapping (Hanusch, 2010, p. 5)

If digital photos such as those depicted in Figure 3-11a are used for texturing a surface model, a different approach and hence additional considerations are necessary (Hanusch, 2010):

- Camera model (cf. Figure 3-9): Interior (PPA, c, distortions) and exterior (position and viewing direction) orientation of the camera are required to link the content of the image plane Π to the mesh patches.

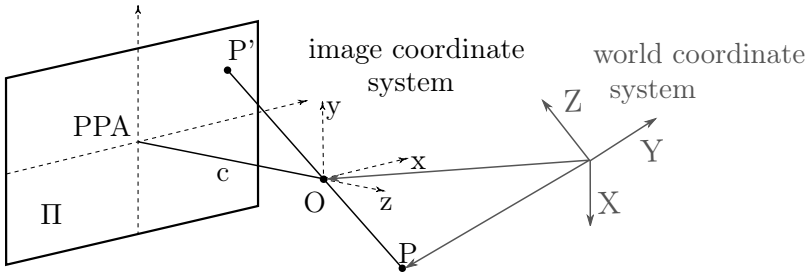

Figure 3-9: Basic camera model for the projection of a point onto the image plane

- Visibility analysis: Viewing direction, focal length and sensor size of the camera are not sufficient to determine which triangles are textured, especially if the object's structure is rather complicated. Some parts of the mesh may be occluded from others from some points of view and thus it is necessary to find out which triangles are actually covered by which image.

  This states a fundamental problem in computer graphics, as every rendering of a scene implies a determination of visible and hidden surfaces (Hughes et al., 2013, p. 1023). By now, two main algorithms have been established: z-buffering and ray-tracing. The former requires, besides the frame-buffer (colour information for every pixel with coordinates x, y), an additional buffer (z-buffer, also called depth-buffer)

with "z-coordinates", which indicates the distance to the screen. For every object, the depth is computed and the colours of the minimum distances are visualised for every pixel (cf. Figure 3-10a).

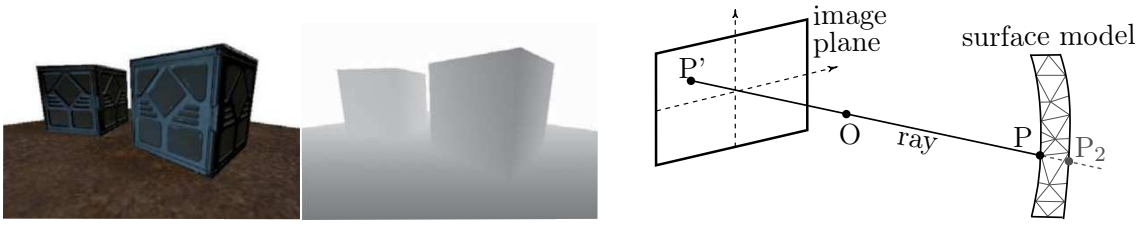

(a) Example of a z-buffer rendered scene and its depth map (Hughes et al., 2013, p. 1036)

(b) Principle of ray-tracing

Figure 3-10: Visibility analysis algorithms used for texture mapping

In the ray-tracing algorithm, every pixel is checked on potential coverage of the mesh. Therefore, a *ray* is defined by two points, the projection centre O and the 3-D point of the pixel to be analysed (lying in the image plane). In fact, the intention is to reconstruct the object point P from the corresponding image point P' by computing the intersection point between the ray and the mesh. In case that more than one intersection point is found, the one with the shortest distance to O is visible (cf. Figure 3-10b).

- Colour correction: If multiple photos are taken for texturing a mesh, radiometric differences should be minimised in order to get a homogeneous photo model. A seamless transition between adjacent textures is achieved by applying different image processing techniques.

  The principle assumption underlying these correction procedures is that the effective colours of overlapping regions differ due to changing incidences of light on the lens. The amount of light captured by a photo may be quantified by the L*a*b* colour space, in which the original Red-Green-Blue (RGB) image is transformed. a* and b* channels describe the pure colour information and the lightness (L) channel approximately corresponds to the human perception of light. Hence, the idea is to establish a matching of the L channel of adjacent textures. This is achieved with Contrast Limited Adaptive Histogram Equalization (CLAHE), which is applied to the L channel, providing contrast enhancement and harmonisation of grey values (here in terms of L values), i.e. a stretching of the image histogram (cf. Figure 3-11c and 3-11d).

  The above described approach minimises the radiometric differences globally, i.e. over the whole image. However, the transition between neighbouring textures may

still not be perfect yet and edge effects between textures occur (cf. Figure 3-11e). A solution to this problem is given by image blending between different texture sources. For overlapping regions, which are found with algorithms described in Chapter 5.1.1, image pyramids are built up and a weighted mean is computed in dependence on the distance to the image borders, i.e. colour intensities in the region of image borders have less impact. An example for image blending of two photos taken of a concrete dam (cf. Figure 3-11a and Figure 3-11b) is depicted in Figure 3-11f. As can be seen, global radiometric differences and the edge effect could be removed, but pixel saturation, due to image recordings against the sun, still poses a problem. Eventually, the stitching process is inverted, i.e. the corresponding blended image is extracted, and used as the source for texture mapping.

(a) Original left image

(b) Original right image

(c) CLAHE applied to left image

(d) CLAHE applied to right image

(e) Stitched images without colour correction

(f) Stitched images with colour correction

Figure 3-11: Results of the colour correction for minimising the radiometric differences of adjacent textures

3.3 Orthographic surface mapping

In Chapter 3.1 and 3.2 the principal approach for surface mapping of e.g. a concrete arch dam with scan and image data is explained. As a result, a photo-realistic 3D model is obtained, which combines 2D texture and 3D geometry information. For convenience, the 3D model is projected orthographically onto a 2D image plane for further processing and evaluation. Subsequently, the resulting image will be referred to as an orthophoto, even though this is not entirely correct in the strict sense.

Distortions may be neglected for small areas, e.g. defect zones, which is why this rather simple method was chosen. The mapping process may be interpreted as a transformation of two right-handed coordinate systems: the global (X, Y, Z) and the local coordinate system (x, y, z), based on the desired projection view (cf. Figure 3-12).

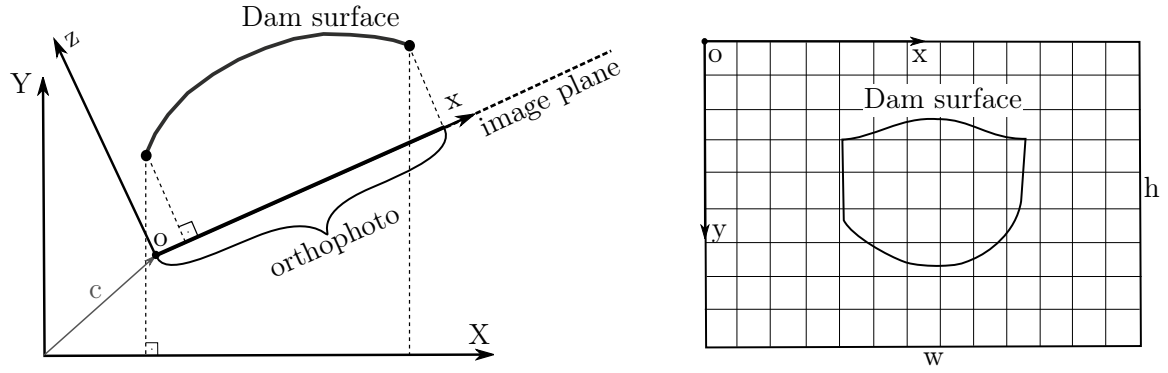

(a) Illustration of the global and the local coordinate system

(b) Dam's surface referenced in the local pixel coordinate system

Figure 3-12: Principle of orthographic mapping illustrated as a coordinate transformation

The transition from the global to the local coordinate system can be described as Helmert transformation

$$\begin{pmatrix} x \\ y \\ 0 \end{pmatrix} = \mu \, \mathbf{R} \begin{pmatrix} X \\ Y \\ Z \end{pmatrix} + \mathbf{c} \,, \tag{3-4}$$

where the z coordinate equals zero as a 3D$\longrightarrow$2D mapping is accomplished. Another important variable parameter is the density of projections lines, which finally defines the orthophoto resolution. Of course, this should be chosen in accordance to texture resolution (m/px), i.e. camera resolution (px) and object-to-camera distance (m). An exemplary orthophoto of a crack on a water dam surface with a resolution of 2mm/px is depicted in Figure 3-2d.

3.4 Scanning and imaging with a state-of-the-art total station

3.4.1 Investigations on scanning functionality

3D laser scanners provide angle and distance measurements, as well as intensity information about the reflected signal. The main mechanical components of 3D laser scanners are a horizontally rotating platform and a deflection mirror rotating about its optical axis. Due to the high rotation speed and sampling rate, state-of-the-art laser scanners are able to measure more than 1 million points per seconds and thus enable extensive point acquisition. On the contrary, total stations are intentionally designed for individual point measurements. However, improvements on motorisation (rotation of telescope about horizontal and vertical axis), measurement speed and data processing encouraged the implementation of scanning routines in the on-board software of state-of-the-art total stations. According to the manufacturer's datasheets, sampling rates from 15 to 1000 Hz are achievable (cf. Leica (2015), Topcon (2016) and Trimble (2015)).

An important factor for the measurement speed is the Electronic Distance Measurement (EDM) technology. While the time-of-flight principle is known for fast unambiguous measurements of distances up to several hundred meters, phase measurements yield measurements with higher accuracy at lower frequency and lower range (Fröhlich and Mettenleiter, 2004).

A combination of both constitutes Wave Form Digitizing (WFD), a technology used in the Multi Stations of Leica Geosystems. In principle, short pulses are emitted at a frequency of 100 kHz - 2 MHz, reflected at the target and received in the telescope, defining a start and a stop pulse. The full waveform is digitised and the time difference between the two pulses is determined. An accumulation of multiple waveforms ensures a higher Signal-to-Noise Ratio (SNR) and hence a better identification of the pulse centres. Besides, the quality of the measurement is influenced by the characteristics of the emitted signal as well (Maar and Zogg, 2014, p. 5): signal amplitude, pulse width and repetition rate. The system parameters are variably adapted in the WFD technology in order to retrieve the maximum of either measurement speed, accuracy or range, or an optimal combination of all three. For this reason, the Multi Stations Leica MS50 & MS60 contain four different scanning modes: 1000 Hz, 250 Hz, 62 Hz and 1 Hz. The achievable distance ranges in each mode are listed in Table 3-1 (Leica, 2015, p. 69), presuming optimal conditions, i.e. measurements perpendicular to a Kodak Grey Card with an albedo of 90%. The same holds true for the measurement noise, which is plotted against different ranges in Figure 3-13 (based on values from Leica (2015, p. 69)). As illustrated, measurement noise increases exponentially even within the specified ranges.

As discussed in Chapter 3.1.2, not only noise but also potential point cloud imperfections have a negative impact on the surface reconstruction process. Therefore, investigations on the Leica MS60 scanning functionality with regard to the mentioned imperfections were performed. The achieved results and insights are presented in the subsequent sections.

Table 3-1: Scanning range limitations of Leica MS50 & MS60 in different modes (Leica, 2015, p. 69)

Mode	**max. Range**
1000 Hz	300
250 Hz	400
62 Hz	500
1 Hz	1000

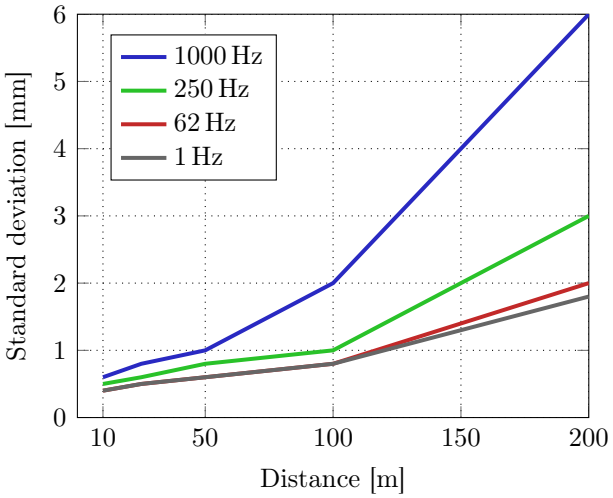

Figure 3-13: Specified standard deviation ($1\,\sigma$) of scan point residuals relative to fitted surface, based on Leica (2015, p.69)

Fröhlich and Mettenleiter (2004) point out that reflectivity properties of the surface's object have a strong impact on the measurement precision. Specific parameters influencing the reflectivity of the laser beam are

- the incident angle of the laser beam on the object
- general surface properties, i.e. material, colour, level of moisture, etc.

Since there are no specifications given by the manufacturer on these factors, empirical research had to be performed in order to quantify the effects on the point cloud data.

Evaluation of measurement noise due to incident angle of laser beam

According to Maar and Zogg (2014), incident angles of 45° or less decrease the measurement quality and hence should be avoided. An experiment was carried out, in which a planar surface was scanned with 1000 Hz from different setup points and hence different incident angles on the object (see Figure 3-14a). Subsequently, a plane was fitted to the point cloud data and the derived deviations were analysed. Results for the observation point with the smallest incident angle (P_4) are presented in Figure 3-15, a summary of the computations for all four points is given in Table 3-2. Note that obvious deviations from the plane were excluded in the computations (points on target plate, cf. Figure 3-14b).

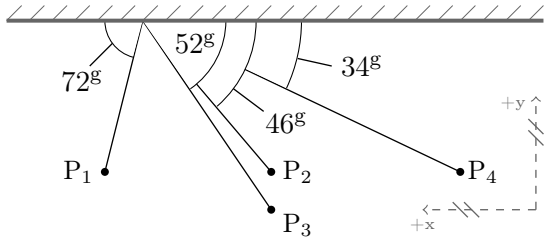

(a) Overview of setup points and incident angles

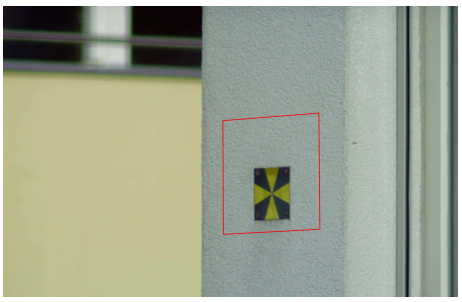

(b) Target surface to be scanned (view from point P_4)

Figure 3-14: Illustration of the experiment setup for testing the scanning precision of a Leica MS60 for different incident angles

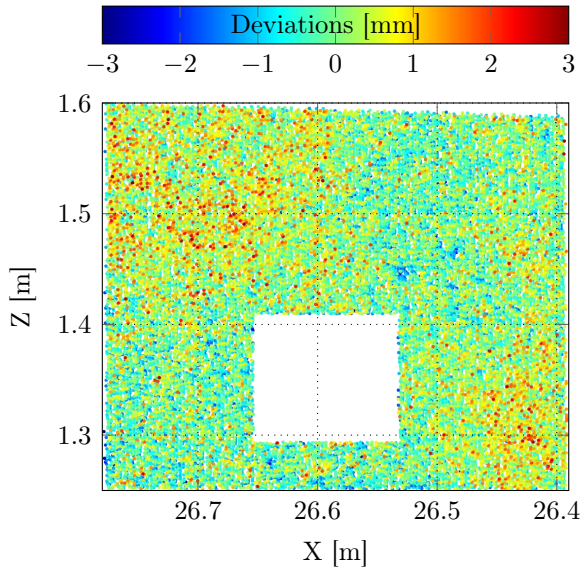

(a) Point cloud deviations with 1 mm spatial resolution (blank area represents the target plate)

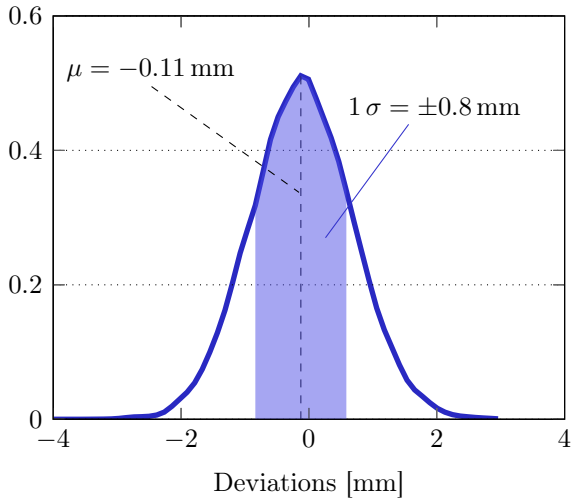

(b) Density function of point deviations

Figure 3-15: Point cloud deviations from a fitted plane for observation point P_4

Table 3-2: Evaluation of measurement noise of the Leica MS60 scanning functionality for different incident angles

point	incident angle [^{g}]	avg. distance [m]	mean of all deviations [mm]	standard deviation [mm]
P_1	72	25.2	-0.1	0.7
P_2	46	35.8	-0.1	0.8
P_3	52	37.4	-0.1	0.8
P_4	34	40.7	-0.1	0.8

Regarding Table 3-2, the investigations revealed no precision loss of the scanning functionality of Leica MS60 due to an increased incident angle on the object. In fact, the noise specification of the manufacturer proved true for a bright planar building wall at the used distances, even at an incident angle of 34^g (cf. Figure 3-13 and Table 3-2).

Evaluation of measurement noise due to surface properties

Recall that in order to assess the quality of scan data of a water dam, its surface properties need to be taken into account. Therefore, an experiment similar to the previous one was performed by acquiring data from the spillway's concrete surface of the Hierzmann dam in Styria, Austria (cf. Figure 3-16a).

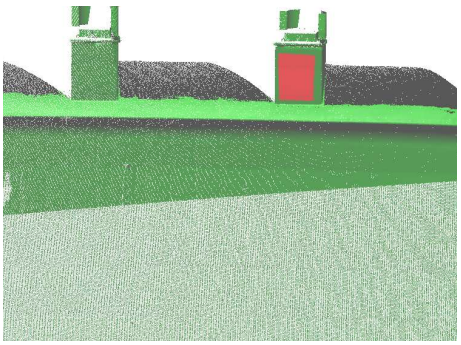

(a) Segmentation (red area) of point cloud data of an arch dam's spillway for plane fitting

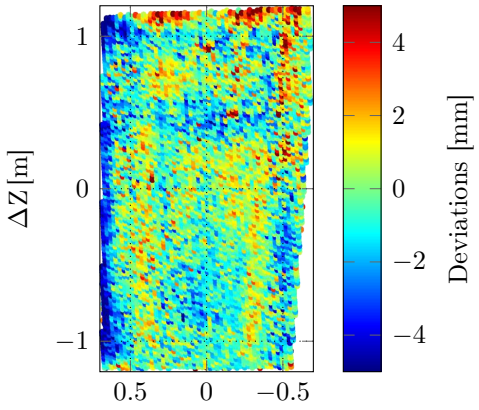

(b) Residuals of point cloud data relative to the fitted plane

Figure 3-16: Evaluation of point cloud noise for a planar concrete surface of an arch dam's spillway (scanning at 80 m distance and 1000 Hz mode)

Although no perfect randomly distributed deviations are provided, i.e. the presumed surface is not absolutely planar, the scan points scatter around the fitted plane with a

standard deviation of 2 mm (cf. Figure 5-5b)). According to the measurement conditions (mode: 1000 Hz, object-to-instrument distance: 80 m), the achieved precision on the concrete surface is perfectly acceptable and does not differ significantly from the specified one on optical targets (cf. Figure 3-13).

However, empirical studies have shown regional differences in the scanning quality for the Hierzmann dam. In particular, dark, moist and partly moss-covered areas, as depicted in Figure 3-17a (dark area), expose a low SNR and hence lead to missing data in the point cloud. Sampled points of such a non-planar surface are evaluated by computing the normal distances from the mesh to the scan points from which it is derived. Figure 3-17b depicts calculated normal distances for one part of the dam. In fact, it shows that there is a big contrast in accuracy between wide parts of the dam and the already mentioned dark areas on the concrete surface. Deviations of 8 mm and more are determined for those areas, whereas an average deviation of 1-2 mm is computed for the major part of the concrete dam's surface.

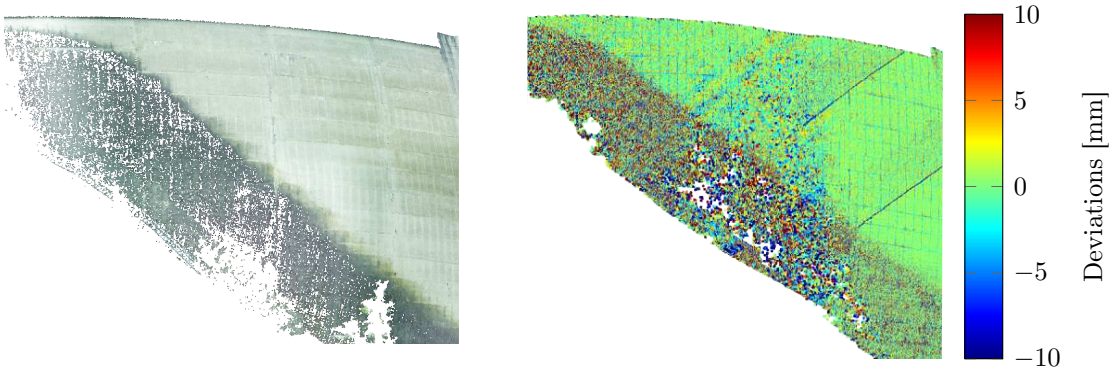

(a) Point cloud with RGB information (b) Computed deviations relative to mesh

Figure 3-17: Evaluation of point cloud noise for different surface finishes of a concrete arch dam

Quality assessment of scan registration from different setup points

Systematic errors like misaligned scan data constitutes a severe point cloud imperfection, complicating the surface reconstruction procedure (see Chapter 3.1.2). At this point, the hybrid instrument Leica MS60 provides a big advantage over terrestrial laser scanners. The classical geodetic station setup routines (e.g. resection) can be used to determine the position of the setup point within an accuracy of 1 mm and the orientation angle within a few arc seconds or better. On that account, registration of scan data from different acquisition points works properly, as Figure 3-18 demonstrates.

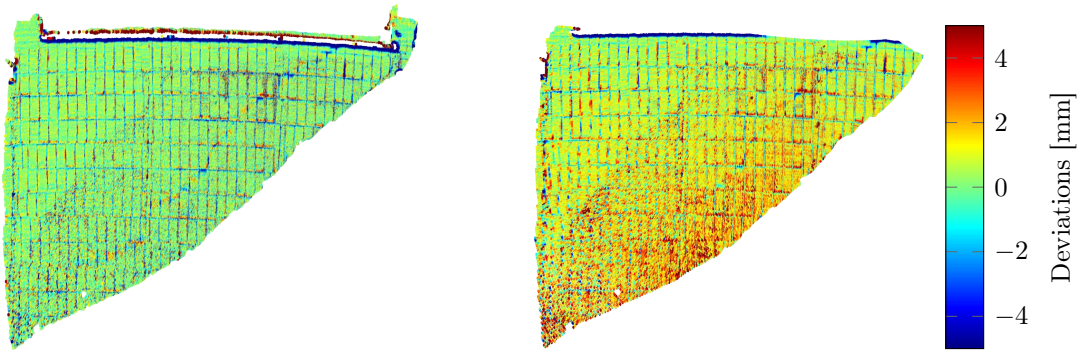

(a) Deviations of scan data from P_1 to the underlying mesh derived from P_1 scan

(b) Deviations of scan data from P_2 to the mesh from P_1

Figure 3-18: Quality evaluation of scan registration for scan data of a concrete arch dam from two different setup points P_1 and P_2

Figure 3-18a depicts the normal distances of a point cloud, which is e.g. measured from a point P_1, to its underlying mesh. Analogously, the deviations are computed from a point cloud acquired from another point P_2 to the same mesh (see Figure 3-18b). The apparent colour difference between the figures indicates an offset between the point clouds. However, the statistical analysis reveals a misalignment of only 0.7 mm (which approximately corresponds to the setup quality) with a similar standard deviation of 2 mm. Considering the data noise due to the measurement distance, which may reach 150 m or more depending on accessibility and size of the dam, and general surface properties (see explanations above), this factor may be neglected for the accuracy considerations of the reconstructed surface model. A prerequisite is that the setup uncertainty (in coordinates as well as orientation) does not exceed the average measurement precision, i.e. 2 mm in the case of a concrete surface being scanned in the 1000 Hz mode.

Overall accuracy assessment of the reconstructed digital surface model

Thus, the overall accuracy for a reconstructed model can be stated, again based on the residuals of point cloud data to the entire mesh. However, an assessment of absolute accuracy requires an independent surface model for comparison. For that reason, the idea has been developed to compare meshes derived from point cloud data of different acquisition dates. By doing so, potential sources of errors such as the following are considered:

- systematic influences due to atmospheric conditions
- blunders in the determination of station coordinates and orientation
- insufficient calibration
- falsification of results due to changing surface properties

Table 3-3: Information on the performed practical point cloud samplings of the Hierzmann dam's surface

	Date	Atm. conditions	Number of points	Mode
Point cloud 1	11-03-2016	$2.5 - 8.4\,°C$ 935 hPa cloudy	2.1 M	1000 Hz
Point cloud 2	11-05-2016	$11.9 - 12.5\,°C$ 929.7 hPa cloudy, partly rainy	2.3 M	1000 Hz

Therefore, surveys at the Hierzmann dam were performed at two different epochs (see Table 3-3). A triangulated mesh based on the point cloud was computed using spatial subdivision with an average grid cell of 0.5 m and a subsequent Delaunay triangulation. For obtaining the final mesh, a facets refinement of 0.1 m was eventually done.

To assess the absolute accuracy, scanning points from epoch 2 (cf. Table 3-3) are compared to the mesh from epoch 1. The resulting point cloud deviations in terms of signed distance information are depicted in Figure 3-19.

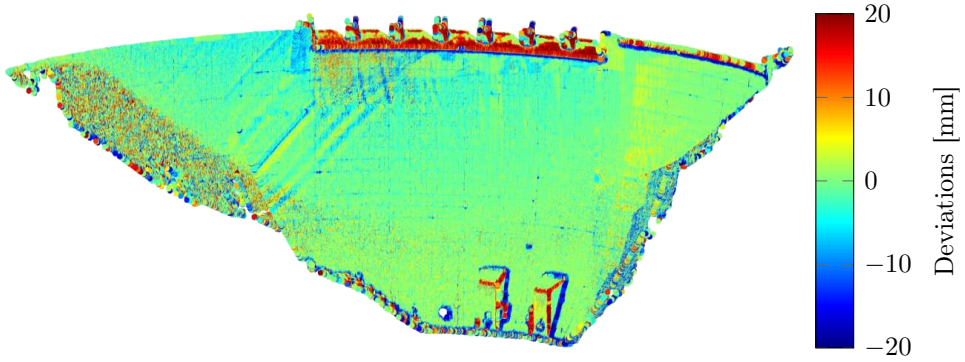

Figure 3-19: Comparison of two point clouds of the Hierzmann dam acquired at different times; illustrated are deviations of point cloud 2 relative to mesh derived from point cloud 1

Other than the increased measurement noise at the dark, moist and moss-covered area on the left-hand side of the wall of approximately 8 mm (cf. Figure 3-17), larger deviations of $\pm 10 - 20$ mm are noticeable at areas with sharp edges (e.g. spillway). The digital reproduction of these edges fails due to the insufficient scanning resolution. However, the mentioned artefacts constitute only a small part of the point cloud, and in fact the computed residuals generally show variations of ± 5 mm (simple standard deviation).

3.4.2 Investigations on imaging functionality

First prototypes of total stations with integrated cameras were developed in the 1980s. By now, many manufacturers have instruments with integrated digital cameras in their product porfolio (cf. Leica (2015), Topcon (2016) and Trimble (2015)). The primary purpose of the cameras is to enhance the surveying process, either by documentation or by image-assisted surveying, which is why these instruments have been termed IATS.

The Multi Station Leica MS60 offers two cameras: the Overview Camera (OVC) and the On-Axis Camera (OAC). The latter is also referred to telescope camera, as it captures the optical path of the telescope. The OVC is a wide-angle camera with fixed focus and a large FOV located above the telescope (see Figure 3-20a), whereas the OAC has a small FOV but benefits from the telescope's 30× magnification, providing image content rich in detail. Photos taken by either camera can be used for texture mapping (cf. Chapter 3.2).

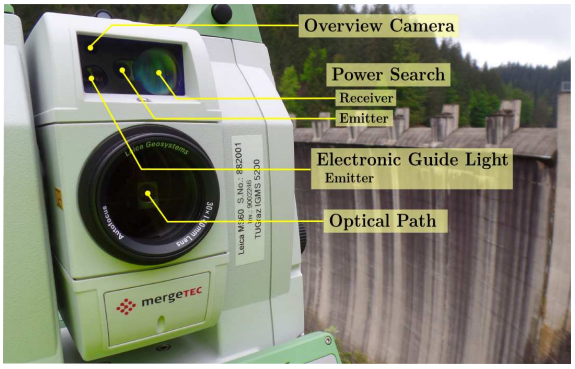

(a) Important components of a Leica MS60 Multi Station

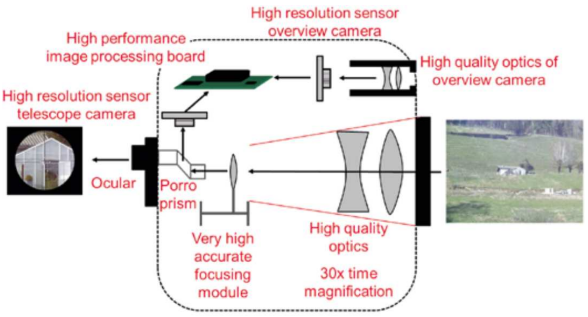

(b) Schematic cross section of telescope structure (Grimm and Zogg, 2013, p. 8)

Figure 3-20: Imaging with Leica MS50 & MS60

Table 3-4: Specifications for Micron MT9P031 CMOS sensor (Micron, 2006)

Optical format	**Active imager size**	**Resolution**	**Pixel size**	**Frame rate (640 × 480)**
1/2.5-inch (4:3)	5.70mm x 4.28mm	5 MP: 2560 × 1920	2.2 × 2.2 μm	20 Hz

Figure 3-20b depicts a cross sectional view of the telescope, in particular of the mechanical components which are introduced for imaging. A Porro prism is installed for splitting up the incoming light source from the telescope into one part being directed onto the sensor and one part towards the ocular. Hence, on the contrary to earlier prototypes, operating the ocular of the telescope while imaging (taking photos and videos)

is possible now. Both cameras use separate, but equal in type CMOS image sensors (see Table 3-4) for image projection.

An important factor for the 3D photo model's quality is the texture resolution Δt, which mainly depends on the image sensor's resolution n_p (number of pixels in width/height), FOV and object-to-instrument distance d.

$$\Delta t = d \cdot \sin \frac{\text{FOV}}{n_p} \tag{3-5}$$

The ratio of FOV and n_p corresponds to the angular resolution of one pixel and may be derived from the manufacturer's datasheet as 6.8 mgon / px for OVC and 0.6 mgon / px for OAC. Empirical studies on the telescope camera have approved an angular resolution of 0.6059 mgon / px (Ehrhart and Lienhart, 2015). Key features for both cameras are listed in Table 3-5 and typical images taken from OVC and OAC are depicted in Figure 3-21.

Table 3-5: Camera specifications for the OVC and the OAC of a Leica MS60

	OVC	**OAC**
Focal length	21 mm	231 mm @ focus ∞
Focus	2 m – ∞ fix focus	1.7 m – ∞ auto focus
FOV	$17.2^g \times 13.0^g$ 27 m × 20 m @ 100 m	$1.4^g \times 1.1^g$ 2.3 m × 1.7 m @ 100 m
Angle Resolution per pixel	6.8 mgon / px 10.6 mm × 8 mm @ 100 m	0.6 mgon / px 0.9 mm × 0.9 mm @ 100 m

(a) Scene captured with OVC; red rectangle illustrates FOV of OAC

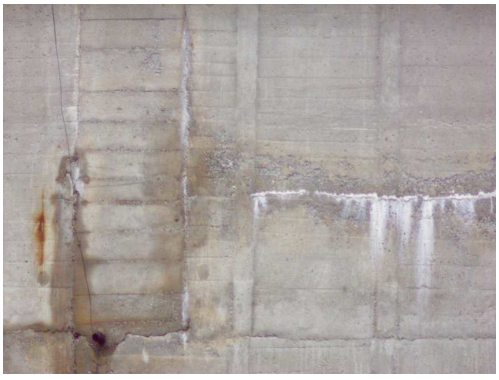

(b) Detailed extract of red rectangle, captured with OAC

Figure 3-21: Example of images captured with OVC and OAC of Leica MS60

Camera model parameters of an IATS

A vital aspect for obtaining high-quality results is a correct camera model, ensuring exact placement, size and orientation of the textures, e.g. of photos depicted in Figure 3-21, on the triangulated mesh. The camera model describes the conversion of pixel coordinates into rays, which are e.g. used for photogrammetric evaluation or, as in the present study, for intersection with the surface model (Chapter 3.2). Interior orientation of the OVC and the OAC, i.e. the internal geometry of the cameras, is given by the following parameters:

- The focal length is the perpendicular distance from image plane to the projection centre and is often denoted as c (cf. Figure 3-9). The focal length of the OVC is calibrated by the manufacturer and presumed to be constant, whereas it varies for the OAC with respect to the distance of the focusing module (cf. Figure 3-20b). The focal length of the OVC can be read via the GeoCOM command `OVC_ReadInterOrient`, but for the OAC there is no such equivalent.

- Theoretically, the point of origin or Principle Point of Autocollimation (PPA) represents the intersection point of the optical axis and the image plane. For the Leica IATS, the principal point corresponds to the crosshair, i.e. the optical axis of the telescope depicted in the image (point P' in Figure 3-22a), displayed for infinite distance. This definition assumes that the viewing directions of both the telescope and camera are parallel, which in fact is not entirely correct (see later in this chapter). The point of origin is referenced in the pixel coordinate system ((0,0) in the upper left corner) and constant for the OVC but variable for each image taken by the OAC, due to changeable focus lens position.

- As outlined above, the viewing direction of the camera and telescope do not coincide exactly. The tilt $\omega\,(\varphi,\, \vartheta,\, \kappa)$ of the image plane Π is described in terms of rotation angles around the axis of the image space coordinate system (see Figure 3-22b). Note the difference between the pixel coordinate system ($\mathbb{R}^2$) and the image space coordinate system ($\mathbb{R}^3$). The rotation angles φ, ϑ, κ are determined for each camera during production and saved internally to compensate for non-parallelism.

- Another parameter to be considered, noting that it affects the internal geometry, is the offset $\vec{o}\,(x_o,\, y_o,\, z_o)$ of the theodolite centre w.r.t. the projection centre O (cf. Figure 3-22a). This parameter is calibrated during production for both cameras and should not change significantly over time.

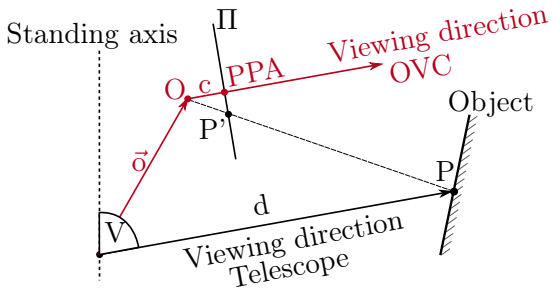

(a) Cross-sectional illustration of the camera position and the orientation

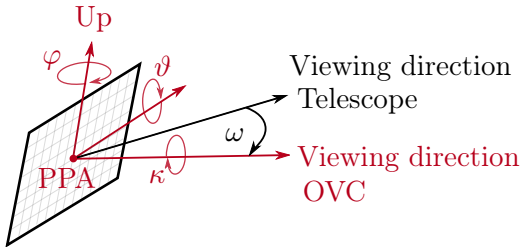

(b) Tilt of the camera viewing direction w.r.t. to the optical axis of the telescope

Figure 3-22: Illustration of the interior orientation parameters for the OVC

Exterior orientation parameters specify position and orientation in space and thus are different for every photo and video frame respectively. The following parameters have to be considered:

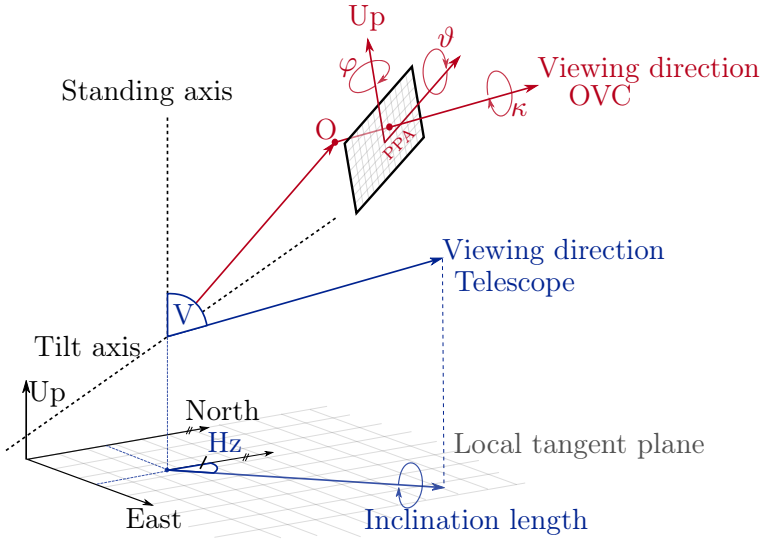

Figure 3-23: Illustration of the complete camera model for OVC of a Leica IATS

- The projection centre O is required in the local coordinate system (Northing, Easting, Height), i.e. the system where the IATS is set up. O can be derived from the station coordinates and the camera location $\vec{o}$ in accordance to horizontal and vertical angles (cf. Figure 3-23). For determining projection centre O, GeoCOM commands `GetStation` and `GetCamPos` are called respectively.

- The viewing direction of the OVC, as depicted in Figures 3-22 and 3-23, is returned in terms of a normalised vector when calling `GetViewingDir`. Starting at the PPA, the direction of the tip is influenced by Hz and V angle on the one hand and compensator values and image plane tilt on the other hand.

In case of Leica MS50 or MS60, all above-mentioned parameters can either be read via GeoCOM commands or exported on-board to a LandXML file. The principle structure of such a file is described in Chapter A.

Texture quality of 3D photo model

In order to assess model quality and the practical value of the approach presented in this thesis, empirical investigations were carried out.

For a homogeneous representation, adjacent textures need to be well-aligned. Hence, a high relative accuracy of textures on the surface model is required. In other words, RGB values of the pixels in the overlapping regions should match, regardless of radiometric differences. The extent of matching is quantified by so-called *image matching* algorithms, commonly used in the field of computer vision and photogrammetry. A more detailed explanation on image matching is provided in Chapter 5.

For the Hierzmann dam, orthophotos of the surface model textured with one OVC image (cf. Figure 3-24a) and its neighbouring ones (cf. Figure 3-24b) were considered. Significant points, also termed key points, are computed for each image and potential correspondences are found (cf. Figure 3-25a). Both scenes are projected orthographically on the same image plane (cf. Chapter 3.3) and thus corresponding points should have the same coordinates. However, slight deviations occur, as Figure 3-25 demonstrates. The arrows indicate direction and magnitude of the displacements (note that their length is scaled for better visualisation). For different textures, the shift can be reliably estimated (red and blue arrows), as all arrows approximately point to the same direction. This hypothesis is approved by the statistics of the 2 groups of key point deviations, listed in Table 3-6. The arrow lengths deviate with 0.4 mm at maximum ($1\,\sigma$). The largest displacement, averaged over all arrows for one group, is computed at 2.8 mm, corresponding to an angular offset of 4 mgon. Considering Table 3-5, the relative accuracy of adjacent textures captured by the OVC is given as less than one pixel.

(a) Textured surface model using single photo

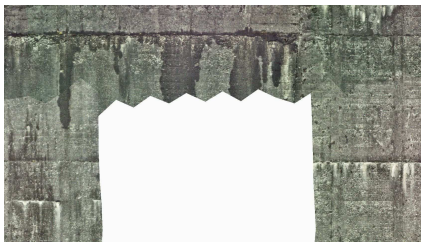

(b)
Surface model textured with adjacent photos

Figure 3-24: Orthophoto of textured surface model with adjacent OVC images taken at a distance of approximately 40 m

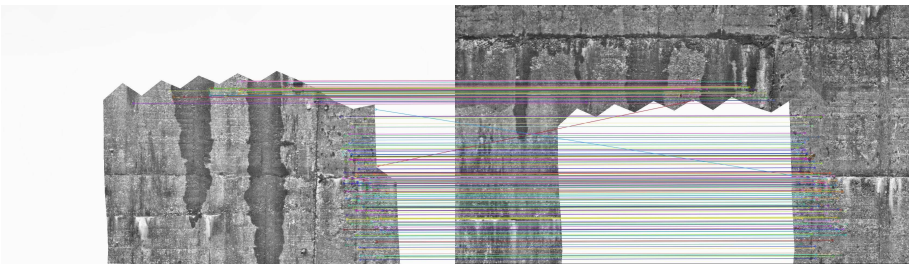

(a) Key point matching of two orthophotos

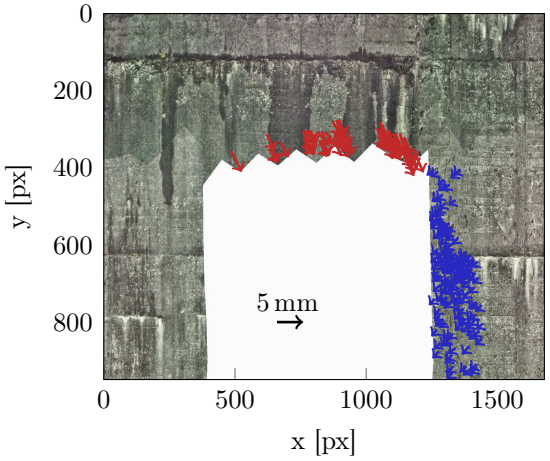

(b) Computed displacement between the orthophotos (arrows scaled by factor 10)

Figure 3-25: Results of image matching and misplacement quantification for adjacent OVC textures on the 3D surface model of the Hierzmann dam

Table 3-6: Statistics of the computed displacements of exemplary adjacent textures on the surface model of the Hierzmann dam

Group	**Deviations in x [mm]**	**Deviations in y [mm]**
Red	1.1 ± 0.2	1.7 ± 0.4
Blue	-2.8 ± 0.3	2.0 ± 0.2

Due to the dimensions and geometry of abutments and the dam itself, data acquisition from multiple setup points may be necessary to cover the whole concrete dam with scan and image data. Therefore, texture coincidence is vital, independent of exterior orientation. Figure 3-26 compares the original images and the final orthophotos of the photo model textured with the former from different observation points. The procedure described above is used to find corresponding points in both images and hence to compute the deviations, which are depicted in Figure 3-27a.

(a) Original image captured from P_1

(b) Original image captured from P_2

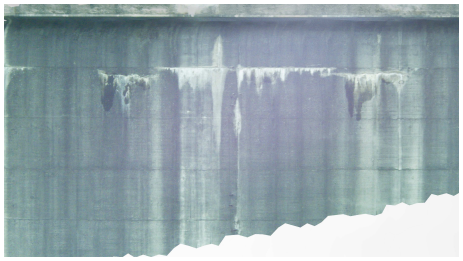

(c) Orthophoto of the 3D photo model, textured with the image from P_1

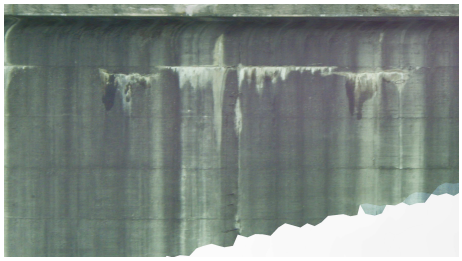

(d) Orthophoto of the 3D photo model, textured with the image from P_2

Figure 3-26: Comparison of raw OVC images and resulting orthophoto after texture mapping from different points of view

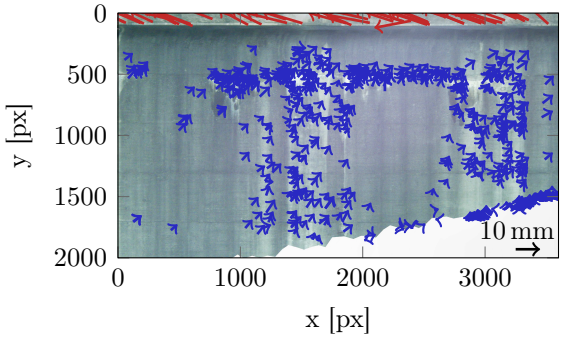

(a) Key point displacements between orthophotos of textured mesh

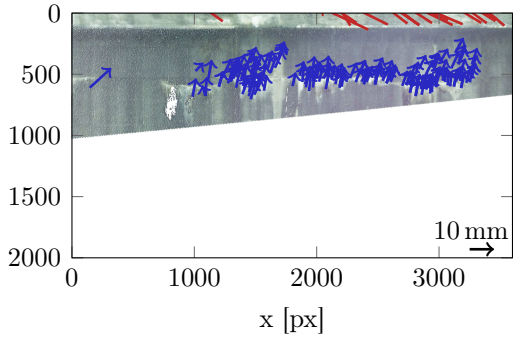

(b) Key point displacements between orthophoto of textured mesh and scan with RGB values

Figure 3-27: Evaluation of OVC texture displacements for different setup points and relative to a RGB point cloud

Despite some outliers, it may be assumed that all arrows point in the same direction, which is actually not the case. In fact, two different groups of deviations were derived (red and blue arrows). In brinciple, the red group results from distortion effects of the textures being mapped on the surface and thus these results should be rejected. The blue group reveals an average displacement of 5 mm, which represents, considering setup and angle uncertainty with an average object-to-instrument distance of 60 m, a fairly sufficient relative texture mapping accuracy (corresponds to less than one pixel for OVC).

To evaluate the absolute texture accuracy, i.e. whether all orientation parameters were considered correctly, the following approach was considered. Prominent features on the dam, i.e. defects like efflorescence, are apparent in the point cloud's intensity and RGB values. The RGB values result from colouring the scan points with the stitched panorama images on-board. The correct colouration is verified visually with the intensity values at regions of interest.
Now, the coloured point cloud is mapped orthographically on the image plane and key points are computed, analogous to the approach for the textured mesh (cf. Figure 3-25). For the purpose of matching the textured mesh's orthophoto with the point cloud (acquired from the same observation point), an adaption of the point size for visualisation might be necessary to generate an almost continuous image (without too large holes). Notably, the aforementioned distortion effects are equally visible in the depicted deviations of matched key point coordinates of both the scanned and textured mesh. The average arrow length of the blue group, i.e. the offset for textured mesh and RGB point cloud, was found to be 15.8 mm. This rather large offset, which corresponds to 15 mgon at an object-to-instrument distance of 60 m, may be attributed to incorrect camera parameters. Regarding these parameters, the camera's factory settings have been used in this thesis. Camera calibration before data acquisition will likely mitigate this offset.

As outlined in Chapter 2, defects on a concrete dam, e.g. sinter formation and cracks, are captured with the OAC and thus different parameters need to be considered for detailed documentation. Similar considerations to the above mentioned investigations for texture quality analysis using OAC images are therefore necessary.

One defect section on the Hierzmann dam was captured in terms of an array of OAC images with 40% overlap, acquired via GeoCOM. Every second horizontally consecutive image was taken for texturing, which resulted in an incomplete photo model (cf. Figure 3-28a). The complementary textured surface model is obtained by repeating the procedure but starting at the first skipped texture (cf. Figure 3-28b). Deviations of matched key points in the orthophotos of the two surface models, which are depicted in Figure 3-28c, are averaged over all overlapping regions. At large, it shows that the expectation (mean value) of adjacent texture displacements is infinitesimal when considering a representative number of OAC images. The 1σ standard deviation of 0.2 mm, expressed in terms of angle uncertainty, gives 0.4 mgon, which constitutes less than one pixel for OAC images (cf. Table 3-5).

The already described test setup for testing scanning accuracy for different incident angles (cf. Figure 3-14) was simultaneously used to assess the relative texture accuracy from different observation points. The target plate represents the only area providing prominent features in the image (cf. Figure 3-29a). This generally is a prerequisite for

feature-based image matching methods. The orthophoto of the mesh textured from P_2 was used as a reference for texture mapping and the computation of key point deviations. An example for P_3 is depicted in Figure 3-29b. A summary for all combinations (P_2 - P_1/P_3/P_4) is given in Table 3-7.

(a) Orthophoto of a surface model textured with every second consecutive OAC image

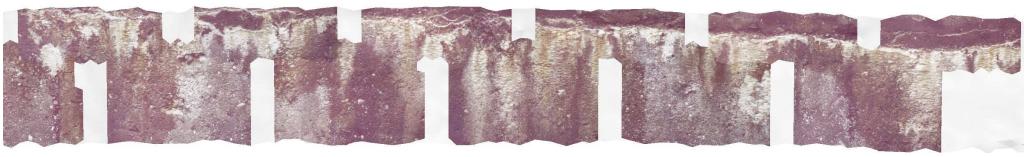

(b) Orthophoto of the complementarily textured surface model

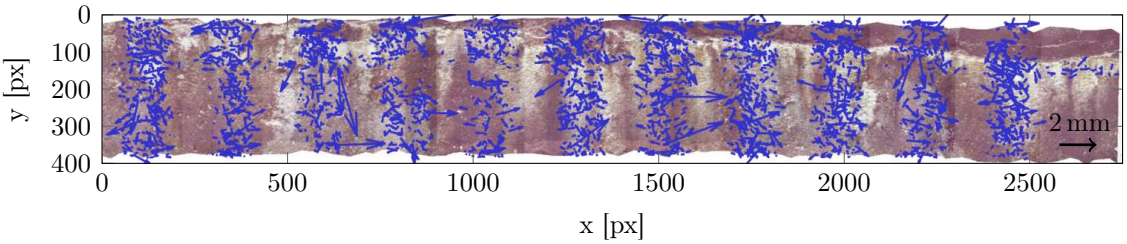

(c) Key point deviations of the orthophotos from complementarily textured surface models

Figure 3-28: Evaluation of the relative texture accuracy for OAC from orthophotos of a defect on the downstream side of the Hierzmann dam

(a) Original OAC captured from point P_3

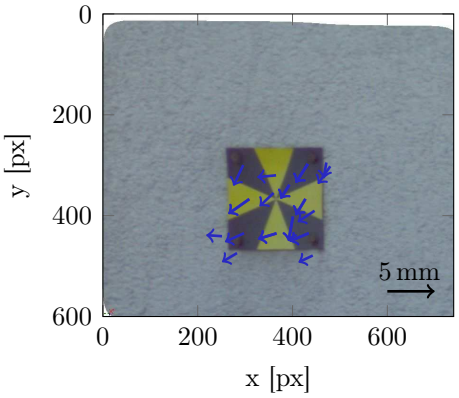

(b) Orthophoto of surface model textured with OAC image from P_3 and superimposed with displacements relative to orthophoto from P_2

Figure 3-29: Evaluation of OAC texture displacements for different setup points

Table 3-7: Statistics of computed key point displacements for OAC images captured at different setup points

combination	mean of all displacements [mm]			standard deviation
	x	y	norm	of norm [mm]
P_2-P_1	0.6	0.4	0.7	0.4
P_2-P_3	-0.6	0.5	0.8	0.1
P_2-P_4	1.0	-0.25	1.0	0.5

According to Table 3-7, texture displacements of 1 mm or less have been determined, which mainly result from setup uncertainty. The estimated standard deviations of the key point displacement are slightly higher compared to those of adjacent textures presented above. As a matter of fact, this has less to do with the acquisition point or the incident angle than with the image content. Images rich in prominent features provide good matching results and hence precise and reliable key point deviations. An average number of 20 outlier-cleaned matched key points, mainly detected on the target plate, is opposed to hundreds of available key points, identified between just two textures of a crack on the Hierzmann dam (see Figure 3-28).

Due to the low image resolution of the panorama image, which is used for colouration of scan points, a quantification of absolute accuracy of OAC textures based on matching with the RGB point cloud is, in contrast to OVC textures (cf. Figure 3-29b), not possible.

3.5 Conclusion

In the last sections, all necessary modules for the proposed workflow (cf. Figure 3-1) for surface documentation of a water dam with scan and image data, originating from an IATS, have been explained. The final outcome, a textured 3D model, combines geometry and image information such that a correct digital representation of the whole concrete wall is provided, independent of viewing direction and position. Mapping the 3D photo-model onto a plane for orthophoto generation is possible without information loss (position, orientation and spatial resolution is known) and yields additional benefits as well. This way, defects on a concrete dam's surface can be surveyed and monitored using orthophotos only.

The major insights in surface mapping with an IATS are summed up as follows.

Lighting conditions affect shots by any camera. As water dams usually are located in mountain valleys, sunlight and shadows are ever-present and hence pose key challenges for deriving homogeneous textures (cf. Figure 3-30). Regions illuminated by sunlight deliver appealing results whereas shadowed regions and image acquisitions against sunlight yield dark and saturated pixel regions on the digital surface model. However, this affects wide-angle images with a large FOV (e.g. OVC of Leica MS50/60) more than high-resolution images of defects (e.g. captured with a telescope camera).

Figure 3-30: Orthophoto of a textured 3D model of the Drossen dam

Variable texture resolution saves processing time and resources. For an overview orthophoto (cf. Figure 3-30) of the whole surface, OVC textures are sufficient. Nonetheless, a spatial texture resolution of 0.6 mm, as has been achieved with an inspection drone for the Tseuzier dam (cf. senseFly (2016)), is equally provided by an IATS at a distance of 65 m for OAC images.

Data acquisition is rather simple, no special expertise of surveyors is needed compared to, for instance, operating an inspection drone. Scans from different observation points are linked by station setups and oriented images are provided by IATS calibration parameters as well as Hz,V and inclination measurements.

Quality of 3D photo-model has been found in Chapter 3.4.1 and 3.4.2 to be considerably good. Investigations on acquired and processed data of the Hierzmann dam from a Leica MS60 have shown an overall geometrical quality of ±5 mm and a subpixel accuracy in texturing. Setup quality, surface structure and the chosen scanning mode are the key parameters influencing the quality of the final result.

4 Automatic in-situ identification and registration of defects

4.1 Image based defect detection

Various types of defects on the downstream and upstream side of a concrete dam have already been considered in Chapter 1.2. The principal human perception of such defects is based on knowledge about their appearance. Cracks, joint openings and sinter formation on a concrete block yield white spots on the surface. Problems with concrete material such as erosion, popouts and spalling, evoke recognisable irregularities on the dam's surface.

These visual characteristics are exploited by the developed algorithm for automatic defect detection. OVC images of the Leica MS60, which were captured for surface mapping (cf. Chapter 3), are used for the analysis. The parameters of interest and their principle approach for image analysis used in this thesis are listed in Table 4-1.

Table 4-1: Approaches for the image based defect detection

Image Characteristics	**Approach**
Brightness	Global thresholding Otsu's binarisation
Visual irregularities	Image gradient Edge detection

4.1.1 Image segmentation

Analysis of brightness

In the case of OVC and OAC, a digital photo with 5 Mpx, i.e. 2560 px in width and 1920 px in height, is captured. Each of these pixels contains 24-bit colour information, composed of 3 channels representing the primary colours RGB with 8-bits (values $0-255$). For further processing, the RGB image, which corresponds to a $w \times h \times 3$ matrix, is converted to a gray-scale image ($w \times h \times 1$) by computing the perceptually weighted mean in OpenCV (Bradski and Kaehler, 2008, p. 60)

$$\mathrm{Y} = 0.2999 \cdot \mathrm{R} + 0.587 \cdot \mathrm{G} + 0.114 \cdot \mathrm{B} \,. \tag{4-1}$$

A photo, captured by the OVC, and its corresponding grayscale image, both covering a scene on a concrete dam, are displayed in Figure 4-1. Those pixels which picture the sintering formation in the central part of the image, have higher grayscale values as

Figure 4-2a illustrates. Based on this insight, a possible approach for identifying defects is to simply filter all pixels, whose intensity values are above a predefined threshold (cf. Figure 4-2b).

(a) Original photo (b) Gray scale image

Figure 4-1: Conversion of a digital RGB photo to a grayscale image

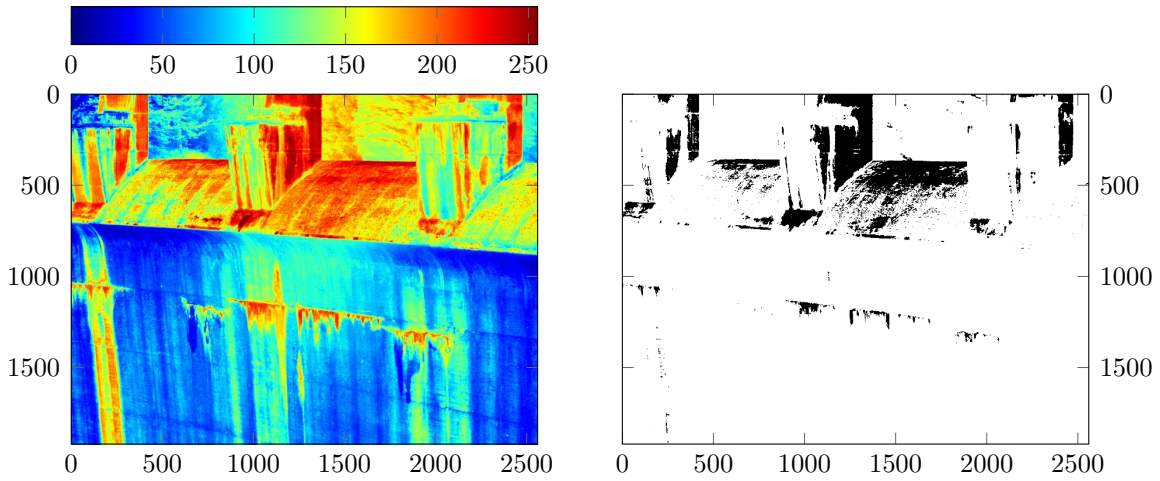

(a) Gray scale image displayed in blue-to-red colourmap (b) Thresholded grayscale image at intensity 220

Figure 4-2: Global thresholding of a grayscale image

As can be seen, a satisfying extraction of the sintering formation is achievable. A drawback of this approach is the manual definition of an appropriate threshold, which is assumed to be different for every single photo.

A solution to this is found in Otsu (1979), where an automatic threshold selection method is proposed. The histogram of a grayscale image I is split up into two classes, whose statistical measure of separability is maximised. Assuming that the image I is composed of N_g grayscale levels $\{1, 2, \ldots, N_g\}$, every level is represented by a number of n_i pixels. The normalised histogram is determined by dividing through the total number of N pixels ($\sum_i n_i$) and may be interpreted as probability distribution (Otsu, 1979, p. 63)

$$p_i = \frac{n_i}{N} \qquad p_i \geq 0 \qquad \sum_{i=1}^{N_g} p_i = 1 \; . \tag{4-2}$$

$N_g - 1$ possibilities of separating the histogram into two classes exist. For each of these possibilities, the probability of occurrence and mean for both classes are computed

$$\begin{aligned} \omega_0(k) &= \sum_{i=1}^{k} p_i & \mu_0(k) &= \sum_{i=1}^{k} i\, p_i \\ \omega_1(k) &= \sum_{i=k+1}^{N_g} p_i & \mu_1(k), &= \sum_{i=k+1}^{N_g} i\, p_i \; . \end{aligned} \tag{4-3}$$

As shown in Otsu (1979), maximising the inter-class variance $\sigma_B^2(k)$ corresponds to minimising the intra-class variance. By doing so, two distinct classes are formed. The optimal threshold k is thus found for $\max_{1 \leq k \leq N_g} \{\sigma_B^2(k)\}$.

$$\sigma_B^2(k) = \omega_0(k)\, \omega_1(k)\, [\mu_0(k) - \mu_1(k)]^2 \tag{4-4}$$

For the initial grayscale image of a water dam, an optimised threshold at a gray level of 168 was found (cf. Figure 4-3a). In contrast to the manual approach (thresholding at 220, cf. Figure 4-2b), far more pixels are detected as potential defects by the automatic image segmentation method (cf. Figure 4-3b). In fact, a lot of pixels with intensities beyond the threshold do not cover the downstream side of the concrete dam at all. An algorithm for filtering those parts of an image which are actually of interest (e.g. downstream side of the dam) is introduced in Chapter 4.1.3.

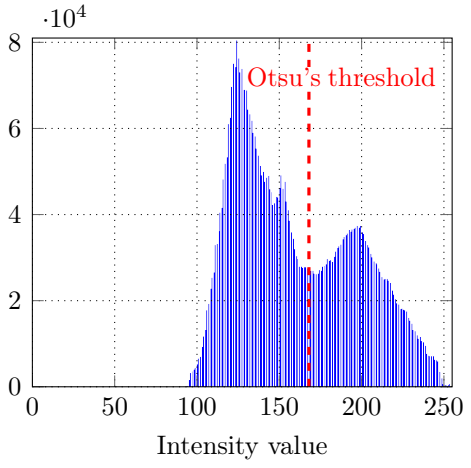

(a) Histogram of the grayscale image

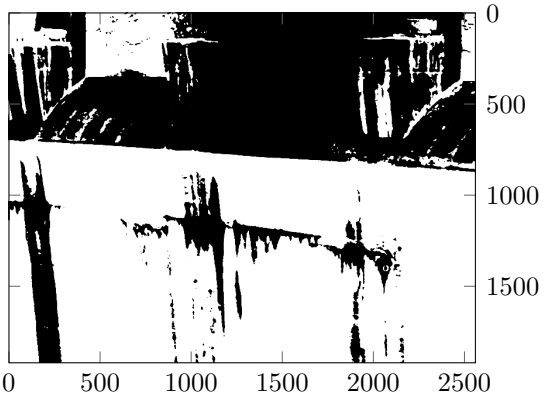

(b) Thresholded image with Otsu's method, threshold: 168

Figure 4-3: Image segmentation with Otsu's method

Analysis of visual irregularities

Instead of using a global threshold, a relative measure for segmenting defects from the background, i.e. from the regular concrete surface, is introduced. A popular approach in computer vision for information extraction from an image is to compute image gradients, which indicate intensity changes relative to its neighbouring pixels. Large intensity changes are therefore assumed to represent visual irregularities on the dam's surface. Foreground-background segmentation is thus achieved by thresholding the gradient image.

From a mathematical point of view, the derivatives are approximated by convolving image I with a filter. According to Bradski and Kaehler (2008), the Scharr filter is preferred to compute gradients in x and y direction respectively

$$G_x = \begin{bmatrix} -3 & 0 & +3 \\ -10 & 0 & +10 \\ -3 & 0 & +3 \end{bmatrix} * \mathrm{I} \qquad G_y = \begin{bmatrix} -3 & -10 & -3 \\ 0 & 0 & 0 \\ +3 & +10 & +3 \end{bmatrix} * \mathrm{I}\,. \tag{4-5}$$

Omnidirectional gradient information is provided by pixel-by-pixel combination of gradient images G_x and G_y in terms of the ℓ^2-norm

$$G = \sqrt{G_x^2 + G_y^2}\,. \tag{4-6}$$

Compared to image thresholding based on grayscale intensities, gradient images are less affected by varying lighting conditions. However, a drawback of this method is its susceptibility to image noise. On that account, high image frequencies are filtered out with Gaussian smoothing first. Figure 4-4a depicts the gradient image of Figure 4-1b after being smoothed with a Gaussian kernel of 15 px × 15 px. The result of image segmentation with a gradient threshold of 230 is shown in Figure 4-4b.

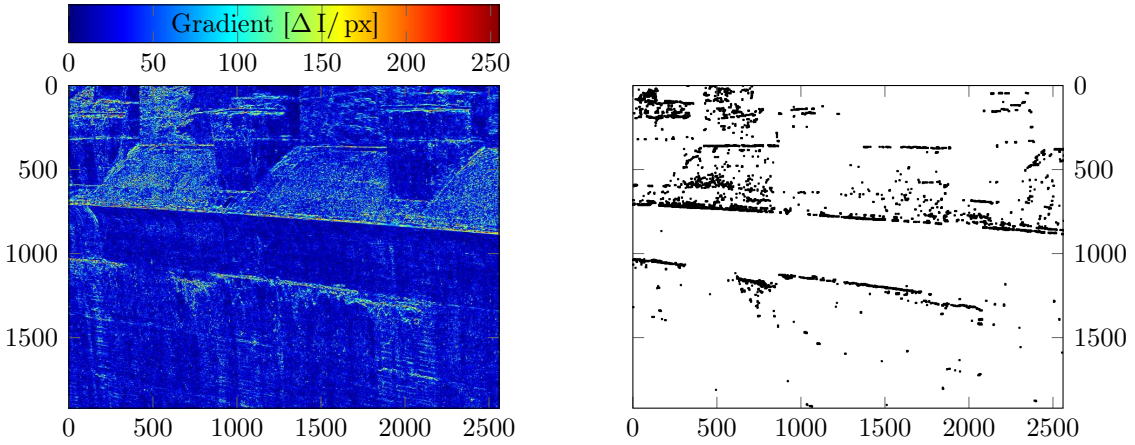

(a) Gradient image

(b) Gradient image segmentation by threshold 230

Figure 4-4: Image segmentation based on gradient thresholding

High intensity changes along a transition line may be interpreted as edges in an image. In case that regular objects are present, e.g. lines and shapes, edge detection algorithms are commonly used to extract features and thus visual irregularities. For the purpose of defect detection, the Canny edge detection algorithm is used in this thesis (Canny, 1986).

This algorithm also uses image gradients that are computed from the Gaussian filtered images with a 5×5 kernel. In addition to the field of magnitudes G (see Equation (4-6)), the gradient direction θ, which is assumed to be perpendicular to edge lines, is computed

$$\theta = \tan^{-1} \frac{G_y}{G_x} \, . \tag{4-7}$$

Consequently, each pixel along the gradient direction (θ is rounded to get four main directions: x, y and diagonals) is checked if it represents a local maximum in the gradient magnitude. Rather than extracting multiple points by thresholding, one representative pixel for an edge candidate along each gradient direction is obtained. In the last step, *hysteris thresholding* is performed to assemble these individual edge candidates into edge lines (Bradski and Kaehler, 2008, p. 152). In principle, two thresholds are supplied in order to find the real edges within all pixels. If gradient values are larger than the upper threshold, the corresponding pixels are specified as *sure-edges*, whereas those pixels coming under the lower threshold are rejected. Pixels, which are between the two thresholds are classified by connectivity, i.e. they are only approved as true if connected to one of the sure-edges.

In Figure 4-5a, the histogram of the gradient image depicted in Figure 4-4a and the thresholds for edge detection are displayed. Compared to the gradient thresholding approach (cf. Figure 4-4b), Canny reproduces the contours better. However, the defects in the central part of the image are detected equally well by both methods.

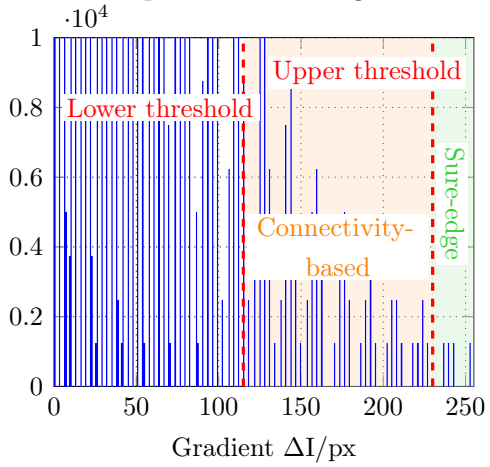

(a) Histogram of the gradient image (y-axis is limited)

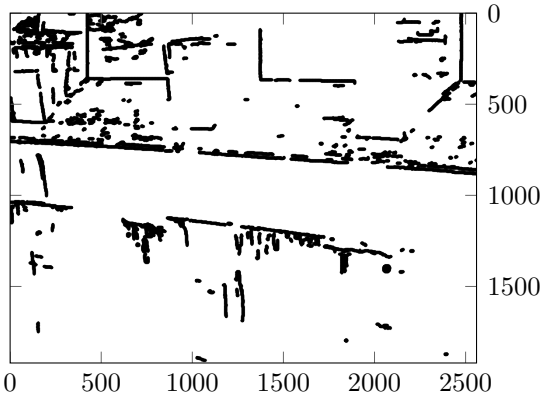

(b) Edges detected with Canny, lower & upper threshold: [115, 230]

Figure 4-5: Image segmentation with the Canny edge detector

Notes on image segmentation from a practical point of view

As illustrated in the last sections, approaches for image-based detection of defects of a concrete dam have been developed and tested. The findings are summarised in Table 4-2.

Investigations on diverse image content have shown that the automatic brightness-based foreground segmentation with Otsu's method is likely to segment too many pixels from the background, i.e. it tends to mistakenly classify image content as critical, rather than missing out any defects. Instead of selecting a threshold for every image manually, Otsu's algorithm is applied as a preliminary procedure for further gradient-based analysis. Pixels filtered out at this stage are most likely not to cover any defects.

Whether the pure gradient analysis or Canny edge detection is chosen, a gradient magnitude of at least $200\,\Delta\mathrm{I/px}$ has been found as a reasonable threshold.

Table 4-2: Synopsis of the segmentation methods for defect detection

Brightness-based method	**Gradient-based method**
Intensity values of pixels covering cracks or sintering areas are higher, thus, thresholding the intensity values is one simple approach for segmenting defects from the rest of the surface.	Image gradients are first derivatives of pixel intensities and therefore describe visual irregularities in an image. Regions with large gradients in a photo of a dam's surface are segmented, as they presumably represent defects.
Otsu's method enables an automatic threshold selection.	This method is independent of ambient light. However, it is susceptible to image noise.
This approach works locally for one image or parts of it, as ambient light strongly influences brightness and hence pixel intensities.	It is a relative method, i.e. transition areas are considered, hence only boundary pixels of potential defects are returned.
Large numbers of pixels may be segmented, resulting in high computational effort of further processing routines.	Canny edge detector proved viable for segmenting regions of interest.

4.1.2 Defect identification

Image segmentation for extracting pixels of interest provides the basis for defect identification. The next step is to group coherent defect areas from representative pixels in segmented images, as shown e.g. in Figure 4-4b. For this purpose, the Density-Based Spatial Clustering of Applications with Noise (DBSCAN) algorithm is used.

In principle, the data clustering algorithm makes use of the intuitive notion of clusters, where the point density is substantially higher inside a cluster than outside (Ester et al., 1996). Therefore, a point p is classified as core point if a number of at least $MinPts$ points are *directly density-reachable* in a ϵ-neighbourhood, i.e. within a distance of ϵ. A point q is denoted as *reachable* from p if there exists a chain of points $p_1, \ldots, p_n$ connecting p and q, in such a way that p_{i+1} is directly reachable from p_i $\forall i$, i.e. which is in the ϵ-neighbourhood. Points are classified as noise if they are no core points and if they are not reachable.

In Ester et al. (1996), a heuristic is suggested for the variables $MinPts$ and ϵ. As the algorithm is applied to the segmented image, these values are presumably constant for approximately similar distances to the concrete wall. Note that the image segmentation process is assumed to yield similar results in terms of feature extraction while rejecting image noise. The result of clustering the segmented image in Figure 4-4b with $MinPts = 80$ and $\epsilon = 60$ is depicted in Figure 4-6.

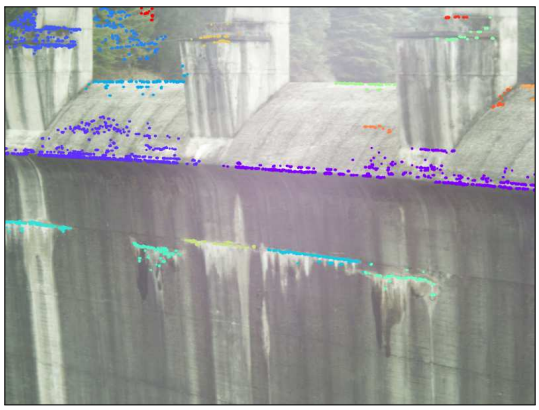

Figure 4-6: Clustering results of the segmented image for defect identification

At this point, representative pixels of each defect on the concrete dam are found and clustered. For the sake of convenience, the MBR is computed of all characterising pixels of a defect.

4.1.3 Geospatial data for algorithm enhancement

The assumptions imposed on the image content for surface evaluation proved true (cf. Table 4-1), as defect detection has been successfully accomplished (cf. Figure 4-6). However, the applied image processing techniques cannot distinguish between the actual concrete surface and other objects, e.g. trees and vegetation, which is why wrongly segmented pixels are also obtained (see upper part of Figure 4-6). Therefore, the idea has been developed to make use of every image's exterior orientation to improve defect identification with the aid of geospatial data. By doing so, the algorithm attains image understanding on the one hand and enables the use of additional information to improve defect identification on the other hand.

Filtering algorithm

On the basis of the segmented image, all pixels inside the polygon representing the outer line of the region of interest are filtered. The characterising points of the polygon are derived from corresponding points in $\mathbb{R}^3$, measured once by the total station for a concrete dam. These points are used for all future surveys, where Hz, V angles are computed for the current station. Using the known camera model for the OVC (cf. Chapter 3.4.2), Hz and V angle are converted into pixel coordinates by the methodology described below.

1. The position of the projection centre O w.r.t. to the station coordinates is read via the GeoCOM command `GetCamPos`. In order to get the absolute location of O, the station coordinates, which are read with `GetStation`, have to be added (Leica, 2014). The camera's viewing direction corresponds to that of the telescope, corrected by the calibrated misalignment angles (cf. Figure 4-7, not to scale).

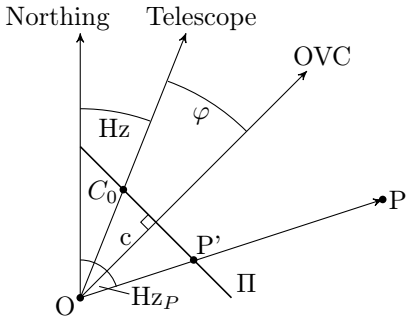

Figure 4-7: Conversion of the physical point P to pixel coordinates

2. Hz_P and V_P (cf. Figure 4-7) are transformed into image space based on the computed coordinates from point O. The difference angles are determined, corrected by the tilt angles φ, ϑ and converted into pixel differences by dividing through the pixel resolution ρ of 6.8 mgon/px (cf. Table 3-5)

$$\begin{aligned} \Delta\mathrm{Hz} &= \mathrm{Hz}_P - \mathrm{Hz} - \varphi & \Delta\mathrm{V} &= \mathrm{V}_P - \mathrm{V} - \vartheta \\ \Delta\mathrm{x} &= \frac{\Delta\mathrm{Hz}}{\rho} & \Delta\mathrm{y} &= \frac{\Delta\mathrm{V}}{\rho}\,. \end{aligned} \tag{4-8}$$

3. These pixel differences correspond to relative image coordinates referred to C_0, i.e. the image position of the optical axis of the telescope. The location of C_0 in the pixel coordinate system is determined with the GeoCOM command `GetActCameraCentre`. The absolute image coordinates of P' are thus obtained by adding C_0 to the pixel differences

$$x_P = x_{C_0} + \Delta x \qquad y_P = y_{C_0} + \Delta y \; . \tag{4-9}$$

Subsequently, the spatial analysis is performed on every pixel to remove those outside the polygon. The proposed filter method's potential is demonstrated in Figure 4-8a, where all coordinates depicted in Figure 4-8b are converted and used to describe the polygon filter.

(a) Illustration of MBR (red rectangles) of detected defects after filtering; cyan line represents the outline of the filtering polygon

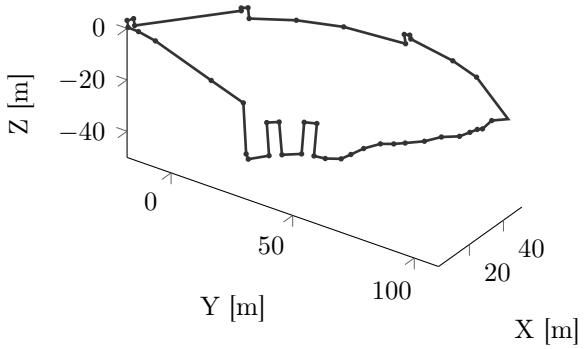

(b) Illustration of the outline of the filtering polygon for the entire Hierzmann dam (in local 3D coordinate system)

Figure 4-8: Geospatial data based filtering procedure for identified defects

Improvement of defect detection

Up to now, defects are identified from one image. However, additional data is assumed to enhance the defect detection algorithm. As images are acquired with an overlap of 40%, a major part of the dam is covered by more than one texture. Moreover, spatial information from the last survey may exist, i.e. coordinates of defects' MBR. An approach for the integration of information from different sources, and hence for improving the results, will be explained hereafter.

Let I^1 be an image, from which MBRs of defects are extracted with the described algorithm. The detection might be incomplete or deficient, and hence an other image I^2 acquired in the course of the current survey, as well as spatial information e.g. from prior surveys, is used. The goal is to get MBRs of defects in terms of Hz and V angles (referred to current station) in the area covered by image I^1. Using the camera model for I^1, the angles are converted into pixel coordinates by applying an operator Ω (cf. Figure 4-9), which implies all computations described above (section "Filtering algorithm").

Spatial information about defects include their extent and position on the dam. The MBR's upper left and lower right coordinates may be available from prior investigations. As emphasised in Chapter 2.2, a reproducible coordinate system is required in order to link data from different epochs properly. With regard to the projection centre O of image I^1 from epoch e, MBR coordinates from e.g. epoch e-1 are used to derive Hz and V angles.

In case that changes have taken place, overlapping or multiple images of the same scene from the current epoch e are preferably used. Overlapping images are linked correctly over image orientation parameters, rather than by stitching images (based on image features). Therefore, the inverse operator Ω^{-1} is applied to the pixel coordinates of detected MBRs in image I^2, which yields the extent of defects expressed in Hz and V angle. Note that the camera model parameters of I^2 are therefore required.

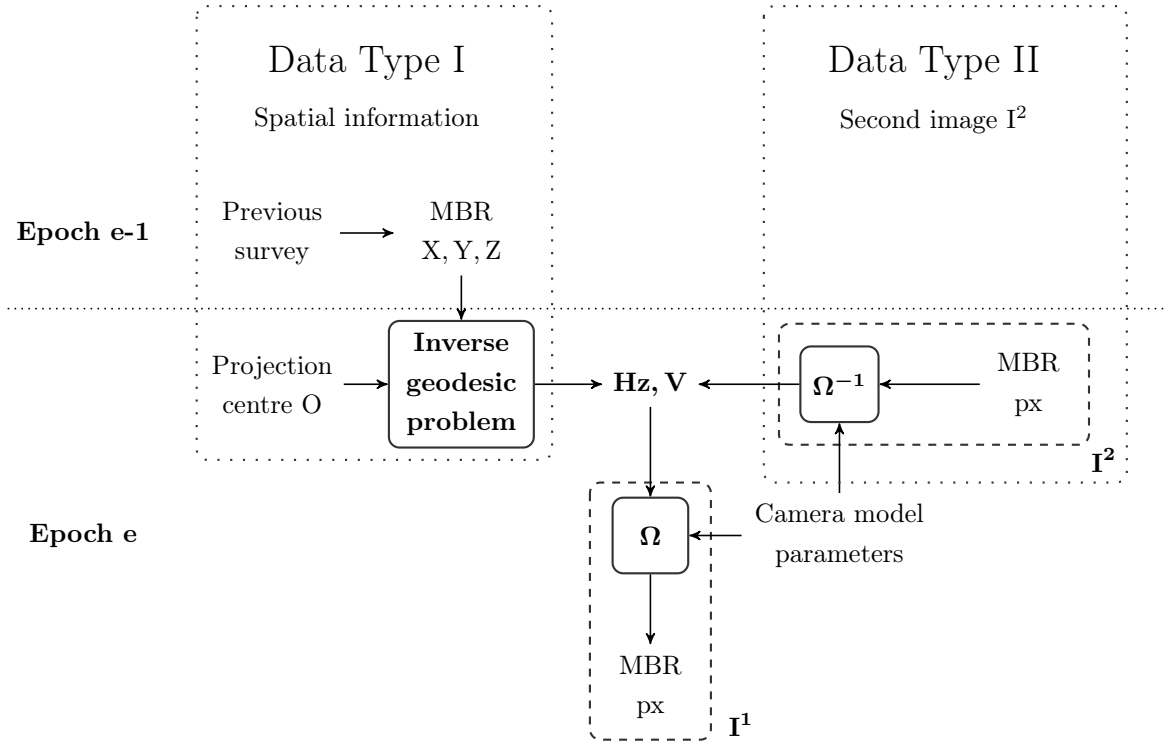

Figure 4-9: Concept for the integration of additional information for enhancing the defect detection algorithm

The potential of additional referenced photos improving the image-based defect detection is demonstrated in Figure 4-10. Two images I^1 and I^2, which cover the same horizontal image content to an extent of 40%, are considered. Concerning defect detection, better results are obtained for the overlapping (dashed) area.

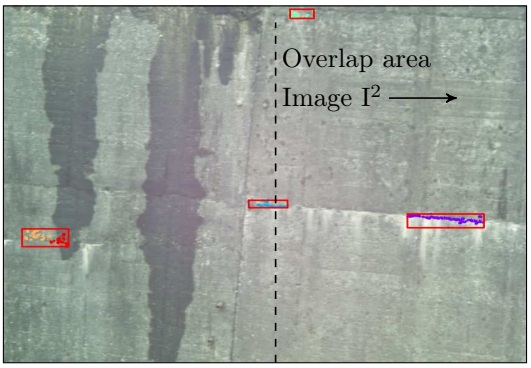

(a) Results of the defect detection in image I^1

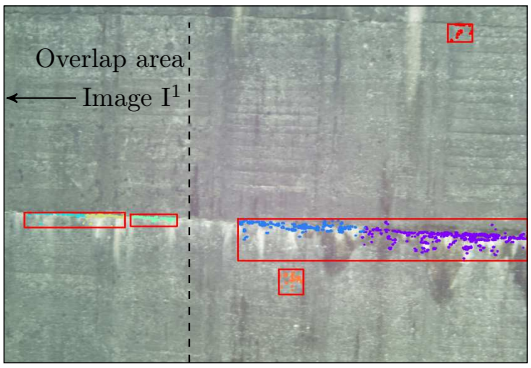

(b) Results of the defect detection in image I^2

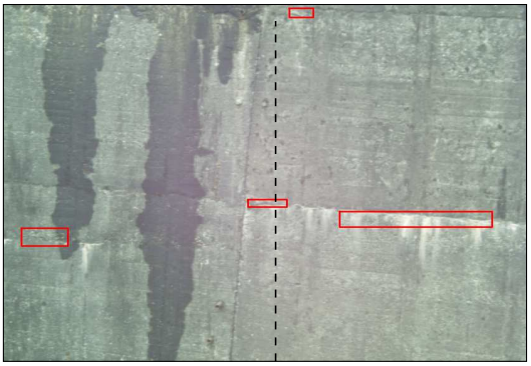

(c) Image I^1 overlayed with the MBR of detected defects from images I^1 and I^2

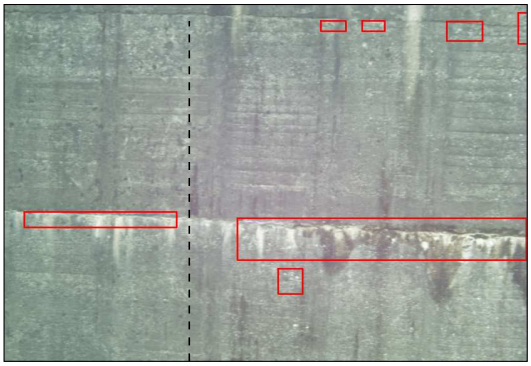

(d) Image I^2 overlayed with the MBR of detected defects from images I^1 and I^2

Figure 4-10: Enhancement of defect detection with a 40% overlapping photo

4.1.4 Evaluation

The proposed approach for defect identification on the surface of concrete dams has proved to work reliably. Regardless of whether image content is taken from different viewing angles (cf. Figure 4-11a) or at different times and light conditions (cf. Figure 4-11b), the actual concrete defects are found. Additionally, other visual irregularities in Figures 4-11a and 4-11b are mistakenly classified as potential defects as well.

Considering two panorama images acquired at two different times (cf. Figure 4-12), the MBR representations of the identified defects may differ considerably. Although the segmentation images look similar, the defects are characterised in a different manner. Information from previous surveys is considered to faciliate a proper spatial identification (panorama images in Figure 4-12 are considered separately).

Occluding objects within the filtering polygon as e.g. vegetation is likely to be classified as defects as well. Therefore, an on-site classification of defects may be performed by the user in an appropriate software interface (cf. Chapter 4.3). For a fully-automatic solution, undesired data may be simply deleted afterwards in the course of the data processing.

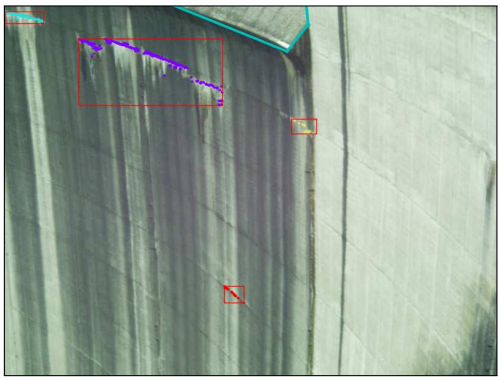

(a) Detection results for a photo acquired from another setup point

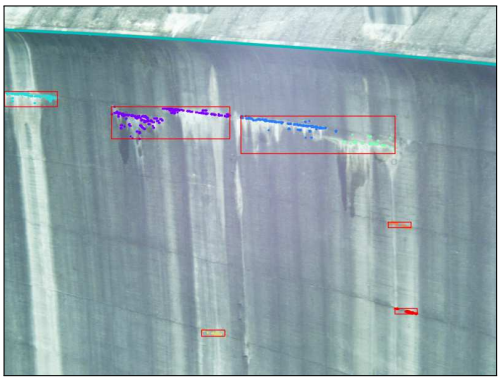

(b) Detection results for a photo acquired under different light conditions

Figure 4-11: Evaluation of detected defects in Figure 4-8b with other OVC photos covering the same scene

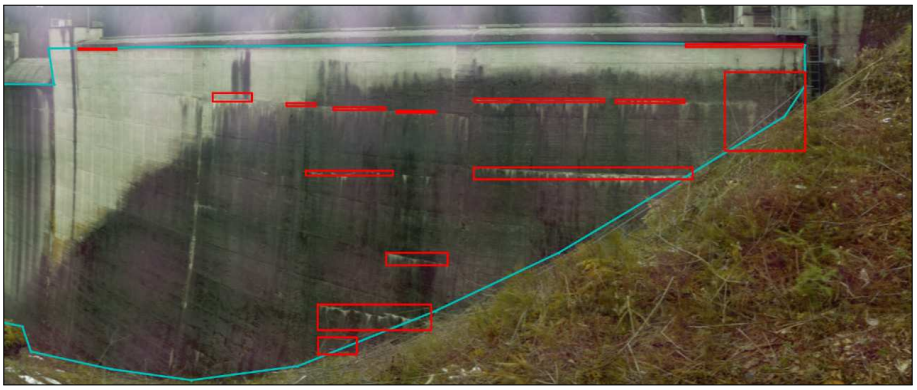

(a) Stitched panorama photo from OVC images, acquired in March 2016

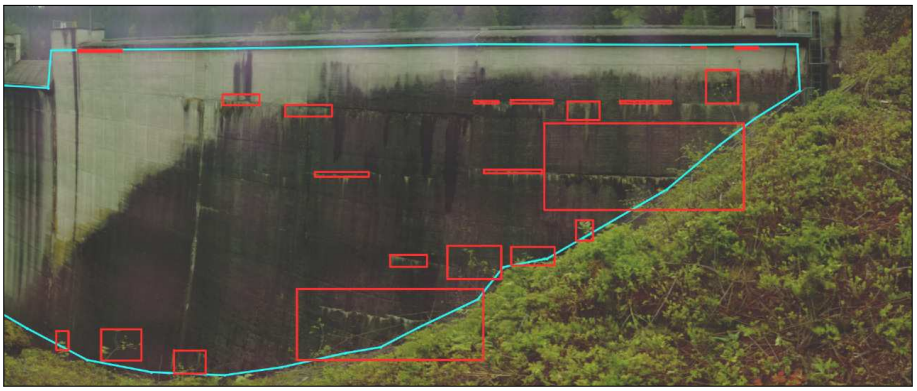

(b) Stitched panorama photo from OVC images, acquired in May 2016

Figure 4-12: Comparison of defect detections based on panorama images from different epochs

4.2 Registration of identified defects

In the previous section, an approach on how to automatically detect defects on a concrete dam's surface has been introduced. It is based on images captured by a Leica MS60 OVC. For the purpose of assessing the current state of the concrete surface, such defects are mapped with the objective to retrieve a high-resolution orthophoto and a textured 3D model. Mapping and documentation of the identified defects requires the on-site acquisition of following data:

- HR point clouds,
- HR photos, captured with the OAC,
- parameters for describing the camera model for each OAC image.

Additionally, notes, photographs and other valuable data of each defect may be recorded as well.

4.2.1 Data acquisition

The extend of each defect is determined by applying the inverse Ω^{-1} operator to the pixel coordinates of the detected MBR (cf. Figure 4-9). Thus, the corresponding Hz and V angles constitute the borders for scanning and image takings. Moreover, the instrument is turned to the upper left (ul) and lower right (lr) Hz, V values to measure the distance (reflectorless) and hence to compute the absolute coordinates, representing the corresponding defect. It has been shown in Chapter 4.1.3 that coordinates are beneficial for future surveys, especially for improving results of the automatic defect detection algorithm.

Regarding high-quality image takings of defects with the OAC, its variable focus and the correct positioning and orientation need to be considered separately. A single autofocus shot is performed to set the focusing module in accordance to the measured distance after positioning the telescope. The positions (Hz_j, V_i) for image captures are computed using the following formulae, noting that they depend on Hz and V at points ul, lr, the degree of overlap θ (e.g. $\theta = 0.2$ for 20% adjacent photo overlap), and the FOV:

$$
\begin{aligned}
\Delta\mathrm{V} &= \mathrm{V}_{lr} - \mathrm{V}_{ul} & \Delta\mathrm{Hz} &= \mathrm{Hz}_{lr} - \mathrm{Hz}_{ul} \\
n &= \left\lceil \frac{\Delta\mathrm{V}}{(1-\theta)\cdot FOV_V} \right\rceil & m &= \left\lceil \frac{\Delta\mathrm{Hz}}{(1-\theta)\cdot FOV_{Hz}} \right\rceil \\
\mathrm{V}_i &= \mathrm{V}_{ul} + i\cdot(1-\theta)\cdot FOV_V & \mathrm{Hz}_j &= \mathrm{Hz}_{ul} + j\cdot(1-\theta)\cdot FOV_{Hz}\ . \\
i &= \{0,\,1,\ldots,\,n\} & j &= \{0,\,1,\ldots,\,m\} \\
n &\ldots \text{number of rows} & m &\ldots \text{number of columns}
\end{aligned}
\tag{4-10}
$$

OAC images may be mapped onto the same triangulated mesh, which has been already derived for an overview documentation of the entire surface (e.g. Figure 3-30). However, the resolution of the underlying point cloud might be too low, especially if data points are averaged for triangulation (as e.g. in 3DReshaper (2016), cf. Chapter 3.1.1). The process of texture mapping assumes that one triangle is completely covered by a texture. However, in the case that the triangles are larger than the image overlapping area on the surface for a predefined distance d, untextured triangles at transition areas of adjacent textures are likely to occur (tested only for 3DReshaper (2016)). In order to avoid such artefacts, the following mathematical relationship is taken into account: For any triangle ΔABC of the mesh, the maximum of all sides $\eta = \max\{a, b, c\}$ is computed. Equation (4-11) establishes the relation between triangle dimension, here interpreted in terms of η, and key parameters for texturing such as object-to-instrument distance d, FOV and the image overlap θ for a perpendicular view.

$$d \cdot \sin\left(\underbrace{n_p \cdot \theta}_{[\text{px}]} \cdot \underbrace{\frac{\text{FOV}}{n_p}}_{[\text{mgon/px}]} \right) = d \cdot \sin\Big(\text{FOV} \cdot \theta\Big) \geq \eta \tag{4-11}$$

Evaluating Equation (4-11) for a dam-to-instrument distance d of 65 m (distance at which a spatial resolution of 0.6 mm is achieved, cf. Chapter 3.5), the triangle extent must not exceed 0.22 m in width or height (assuming perpendicular viewing direction of the OAC).

When recording the image parameters used for defect mapping, the following aspects should be taken into account:

- No information is provided about the position of the projection centre for the OAC, which is why it is assumed to correspond to the intersection point of the optical axis and the standing axis, i.e. to the station coordinates (read with `GetStation`).
- It is assumed that the viewing direction of the OAC is equal that of the telescope, which is defined by Hz and V angle (retrieved by `GetFullMeas`). According to the exported LandXML file, the misalignment angle $\omega(\varphi, \vartheta, \kappa)$ equals zero for the OAC (cf. Figure 3-22).
- The principal point varies slightly with the focusing module. The GeoCOM command `GetCrossHairPos` is used to read it for image takings at any object-to-instrument distance.

4.2.2 Recording of metadata

As part of the surveying process, additional information is recorded about the captured defects:

- **Characteristics of each defect:**
  In addition to orthophotos and textured 3D models, records about type (e.g. crack), properties and particularities of defects provide valuable information to depict the current situation as well as possible.

- **An identification mask:**
  A user-defined boolean variable, which indicates whether a true defect is detected, is stored to the database. MBR coordinates of mistakenly identified regions are measured equally, as they contribute significantly to filtering true defects for future surveys. In practice, the MBR of such regions are transformed into image space and checked on overlap with the detection results from the current epoch.

4.3 Concept for software implementation

In the last sections the functional principle of an automatic defect detection and registration approach has been introduced. A concept for a software implementation is now presented, which shall facilitate and automate these computations.

A software is intended to run on a standard computer or laptop, for operation on-site or via remote access from office. This also depends on the deployment of the surface monitoring solution, i.e. on the option of permanent or selective use (cf. Chapter 2.1).

In principle, the software shall provide algorithms for three major tasks: setting the IATS's orientation, data acquisition and analysis (cf. Figure 4-13). The former two tasks are performed to retrive overview scans and images, and could also be done by the on-board software. However, defect detection requires, as outlined in Chapter 4.1, image processing techniques that can only be performed on an external device. As a matter of fact, the Topcon IS-3 is the only IATS so far which makes use of image processing at all. In the "Feature scan" function of the IS-3, prominent features, i.e. corners, are extracted, which subsequently can be scanned or measured individually (Topcon, 2007).

Following the detections, the software takes control over the IATS and the working circuit is restarted automatically. A fully automated solution from the first to the last step is provided if an interface is established to the defect database. Knowledge based on previous measurements is thereby integrated into the ongoing survey and results from the current epoch are stored into it. As detections rely on a few input parameters, a Graphical User Interface (GUI) is necessary to enable interaction with the operator in order to get optimal results, especially if a dam's survey takes place for the first time.

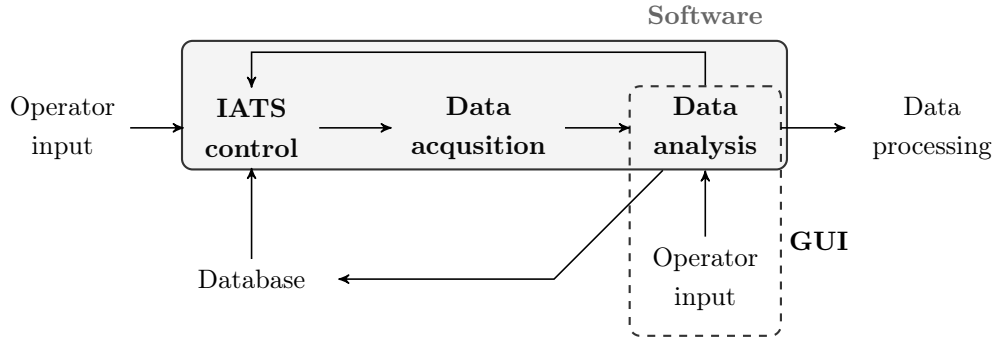

Figure 4-13: Software concept including the interfaces for defect mapping

A proof-of-concept for the usability of a defect management software for operation on-site is given in Chapter B. A user-friendly GUI, which ask for user input as well as an interface to a defect database, is presented.

5 Change detection of surface conditions

The procedure and benefits of the newly proposed method for surface documentation of a concrete dam with an IATS have been outlined in Chapter 3 and 4. Due to the fact that metric information is now provided by the methodology, i.e. by 3D photo models and orthophotos, dimensions of defects, e.g. crack length and width, can be determined. As a matter of fact, all concrete dams are affected by defects to some extent. However, these must never jeopardise the structural integrity of a dam. Therefore, it is important to closely monitor the concrete's state, i.e. survey existing defects and identify new ones.

Regarding the identification of emerging defects, the developed surface monitoring solution (cf. Chapter 2) performs this task automatically at site, as illustrated in Chapter 4.1. Based on orthophotos from different epochs covering the same defect, potential changes are detected in the course of data processing as well. In this chapter, the principles of detecting defects and quantifying their changes using multitemporal orthophotos are outlined.

5.1 Pixel-based change detection analysis

Change detection based on multiple images taken at two different epochs corresponds to a task commonly accomplished in the field of remote sensing. In the past, a broad variety of algorithms have been developed and adopted to deal with multitemporal images of diverse regions and for different kind of applications. Figure 5-1 illustrates the workflow of a change detection analysis at pixel level, which has proven to be suitable for the purpose of monitoring defects on a concrete dam.

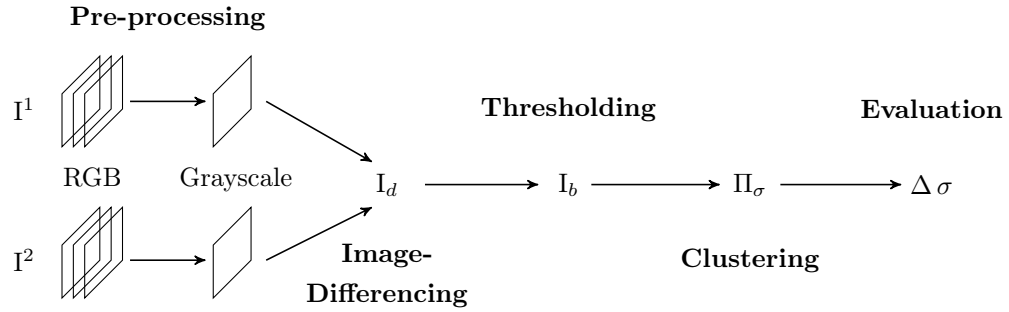

Figure 5-1: Workflow of pixel-based change detection method, based on Niemeyer et al. (2007, p. 2374)

The basic idea underlying the algorithm is that two images I^1 and I^2 depict the same scene and thus should have the same pixel intensities. Consequently, subtracting grayscale intensity values Y of pixels with the same coordinates x, y in both images,

$$\Delta Y^{12}(x,y) = Y(I^1;x,y) - Y(I^2;x,y) \tag{5-1}$$

should equal zero for no-change image regions. By filtering or thresholding the intensity differences, changes can be detected. In practice, however, these assumptions do not necessarily apply, which is why subsequent key steps are required as part of the pixel-based change detection approach.

- Pre-processing and differencing of images I^1 and I^2:
  RGB-to-grayscale image conversion is accomplished first (cf. Equation (4-1)). Afterwards, radiometric normalisation of both images is implemented to minimise global intensity differences. Image to image registration is carried out, ensuring that the correct pixels (a pixel is a sampling of the texture) are taken for computing the difference image I_d.

- Thresholding and clustering:
  Absolute intensity differences, which exceed a predefined threshold, are considered as pixels of change. Analogous to the process of identifying defects, the segmented pixels in a binary image I_b are grouped to get connected areas of change.

- Evaluation:
  Finally, the resulting change map Π_σ is evaluated in terms of relevant measures, i.e. changes $\Delta\sigma$ in unit of length or area.

An elaboration of each step is provided in the following sections. Orthophotos depicting the same defect are analysed, where increasing efflorescence is simulated by placing shaving foam onto the concrete wall (cf. Figure 5-2).

(a) Orthophoto of a defect from epoch e (b) Orthophoto of a defect from epoch e+1

Figure 5-2: Image data for change detection analysis

5.1.1 Image registration

Pixel-based change detection requires textured models of defects to be mapped onto the same image plane (cf. Chapter 3.3). Due to limitations of image resolution, different samplings of the texture lead to image matrices with unequal structure and intensity values (cf. Figure 5-3). Consequently, the difference image I_d would be inaccurate and changes could not be seperated from unchanged regions.

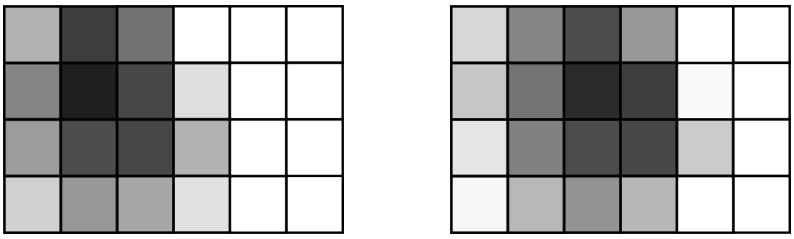

(a) Scene sampled by Image I^1 (b) Scene sampled by Image I^2

Figure 5-3: Schematic figure of two different sampling results of the same scene

Hence, the idea is to align the images by transforming, i.e. by translating, rotating, scaling and stretching, image I^2 to coincide with I^1. This implies that the corresponding coordinates of each pixel centre are considered for the geometric transformation, which can be formulated as

$$\mathbf{X_2}' = \mathbf{A} \cdot \mathbf{X_2} + \mathbf{B} = \begin{bmatrix} x_2' \\ y_2' \end{bmatrix} = \begin{bmatrix} a_{00} & a_{01} \\ a_{10} & a_{11} \end{bmatrix} \cdot \begin{bmatrix} x_2 \\ y_2 \end{bmatrix} + \begin{bmatrix} b_0 \\ b_1 \end{bmatrix} . \tag{5-2}$$

For convenience, the translation vector $\mathbf{B}$ and the complementary matrix $\mathbf{A}$ are formed to one transformation matrix $\mathbf{T}$, where homogeneous coordinates are introduced for $\mathbf{X_2}$

$$\mathbf{X_2}' = \mathbf{T} \cdot \mathbf{X_2^H} = \begin{bmatrix} x_2' \\ y_2' \end{bmatrix} = \begin{bmatrix} a_{00} & a_{01} & b_0 \\ a_{10} & a_{11} & b_1 \end{bmatrix} \cdot \begin{bmatrix} x_2 \\ y_2 \\ 1 \end{bmatrix} . \tag{5-3}$$

Equation (5-3) describes an affine transformation, which is valid for the above described operations, and hence, for images referring to the same image plane. Provided that the local coordinate system is defined equally for all orthophotos to be examined (cf. orthophoto generation in Chapter 3.3), this approach is suitable for the purpose of defect mapping. In the case of different image planes, i.e. different perspectives on the defect, a projective transformation can be applied. Compared to the affine transformation, the mathematical model is described by three more parameters, implying that $\mathbf{T}$ is a 3×3 matrix. The next sections outline how the transformation parameters for affine and projective transformations are determined.

Feature-based approach

The obvious approach is to solve the linear equations presented above for the parameters with at least three corresponding points in both images. In the past, different algorithms for automatically extracting relevant points have been developed in the field of computer vision. One algorithm being commonly used for different kinds of tasks is

Scale-Invariant Feature Transform (SIFT), which produces results invariant to image transformation, varying lighting conditions and affine distortion. In principle, SIFT provides feature detection (step 1-2) on the one hand and feature description (step 3-4) on the other hand. For a more detailed description of the algorithm, the paper Lowe (2004) is highly recommended.

1. Feature detection:
   Relevant points are assumed in the region of blobs, i.e. of distinctive regions in an image. Therefore the blob detector approach with Difference of Gaussian (DoG), in which two blurred images with different Gaussian smoothing kernels are subtracted, is used. DoG is computed for different levels of the image pyramid, for which local extrema are searched (over scale and space).

2. Keypoint localization:
   The location of these extrema is refined using Taylor expansions and potential features are extracted by thresholding the intensity at the refined locations. Due to the high sensitivity of DoG to edges, an elimination procedure is applied to remove sets of points belonging to an edge and hence to obtain distinctive feature points. Keypoints, which were detected for the reference image, are visualized in Figure 5-4.

3. Orientation assignment:
   In order to compensate for image rotation, relative measures, namely gradient magnitude and direction, are computed.

4. Keypoint description:
   A keypoint is characterised by a descriptor, i.e. a 128-element vector. Each element contains the gradient magnitude for a direction of a specific neighbouring pixel. Additionally, the vector is modified to compensate for illumination changes.

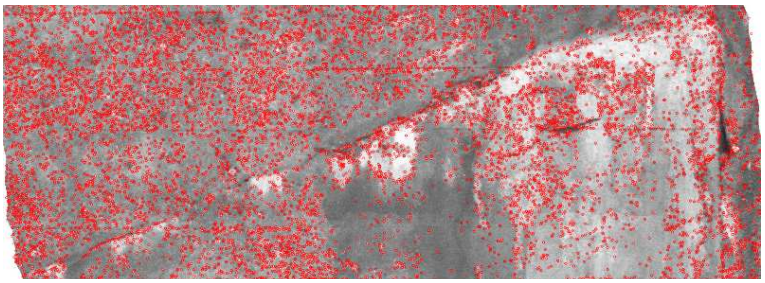

Figure 5-4: Detected SIFT keypoints for an image

As shown in Figure 5-4, a large number of feature points is detected (almost 13 000 for the 1.6 Mpx image), however, the detected feature points might deviate considerably for the other image. Correspondance of feature points from two images is detected by computing and thresholding the eucledian distance of the associated vectors.

Intensity-based approach

Instead of searching and matching distinct points, intensity patterns of a reference image I_r are compared to a warped image I_w: $\mathrm{I}_r(\mathbf{x}) = \mathrm{I}_w(\mathbf{y})$, where brightness constancy, i.e. no overall intensity change of a scene, is assumed. The alignment of images can be interpreted as mapping between image coordinate systems $\mathbf{y} = \phi(\mathbf{x}; \mathbf{p})$, parametrized by a vector of unknown variables $\mathbf{p} = [p_1, p_2, \ldots, p_N]^t$ so that the following relation holds

$$\mathrm{I}_r(\mathbf{x}) = \mathrm{I}_w(\phi(\mathbf{x}; \mathbf{p})) \ . \tag{5-4}$$

The determination of ϕ turns out to be an optimisation problem, where various objective functions have been developed, e.g. targeting the sum of squared differences (Lucas and Kanade, 1981) or the correlation coefficient (Psarakis and Evangelidis, 2008). The latter introduces an enhanced correlation coefficient

$$\rho(\mathbf{p}) = \frac{\bar{\mathbf{i}}_r}{||\bar{\mathbf{i}}_r||} \cdot \frac{\bar{\mathbf{i}}_w(\mathbf{p})}{||\bar{\mathbf{i}}_w(\mathbf{p})||} \ , \tag{5-5}$$

where $\bar{\mathbf{i}}_r$ and $\bar{\mathbf{i}}_w$ constitute zero-mean vectors of pixel intensities of corresponding pixels in both images

$$\begin{aligned} \mathbf{i}_r &= [\mathrm{I}_r(\mathbf{x}_1), \mathrm{I}_r(\mathbf{x}_2), \ldots, \mathrm{I}_r(\mathbf{x}_K)]^t \\ \mathbf{i}_w(\mathbf{p}) &= [\mathrm{I}_w(\mathbf{y}_1(\mathbf{p})), \mathrm{I}_w(\mathbf{y}_2(\mathbf{p})), \ldots, \mathrm{I}_w(\mathbf{y}_K(\mathbf{p}))]^t \ . \end{aligned} \tag{5-6}$$

It can be shown that maximising the correlation coefficient $\rho(\mathbf{p})$ is equal to minimising the objective function

$$E_{\mathrm{ECC}}(\mathbf{p}) = \left|\left| \frac{\bar{\mathbf{i}}_r}{||\bar{\mathbf{i}}_r||} - \frac{\bar{\mathbf{i}}_w(\mathbf{p})}{||\bar{\mathbf{i}}_w(\mathbf{p})||} \right|\right| \stackrel{!}{=} \min \ . \tag{5-7}$$

It is apparent that even if $\mathbf{i}_w$ is a linear function of $\mathbf{p}$, the criterion function is still non-linear due to the vector normalisation (ℓ^2 norm). In Psarakis and Evangelidis (2008), a solution to this rather complex non-linear optimisation problem is found by introducing a sequence of secondary optimisations, which target linearised objective functions.

It has been shown that the proposed iterative scheme converges and thus yields a correct result with reduced computational cost. The algorithm has proved as a good image registration method, provided that deformations are not too large. Moreover, this approach is invariant to photometric distortions in brightness and contrast. The OpenCV implementation `findTransformECC` of this algorithm has been used in this thesis for the alignment of two orthophotos.

Comparison of image registration methods

The resulting transformation parameters $\mathbf{T} = [\mathbf{A}|\mathbf{B}]$ of both methods, SIFT and Enhanced Correlation Coefficient (ECC), are listed below.

$$\mathbf{T}_{SIFT} = \begin{bmatrix} 1 + 105\,\text{ppm} & 72\,\text{ppm} & 0.123 \\ -109\,\text{ppm} & 1 + 204\,\text{ppm} & -0.372 \end{bmatrix}$$

$$\mathbf{T}_{ECC} = \begin{bmatrix} 1 + 73\,\text{ppm} & 36\,\text{ppm} & 0.176 \\ -32\,\text{ppm} & 1 + 334\,\text{ppm} & -0.435 \end{bmatrix}$$

Applying formula (5-3) with $\mathbf{T}_{SIFT}$ or $\mathbf{T}_{ECC}$ to any point inside the image frame $\mathbf{X} = [0 \leq x \leq 2050,\ 0 \leq y \leq 800]^T\ \forall\, x, y \in \mathbb{R}$ leads to results differing by no more than a tenth of a pixel. Hence, both methods are suitable, and the feature-approach (SIFT) is prefered as it requires less computational cost. Nonetheless, in some cases the image content may provide an insufficient number of key points and the computed transformation parameters are thus inaccurate or false altogether. In this case, the pixel-based approach should be used instead.

5.1.2 Radiometric normalisation

After image registration, the coordinate systems of both images are aligned. At this stage, the intensity values might still deviate. Codomain and structure of image matrices might be different due to changing lighting conditions, evoked by different points of view, daytime, season or photo acquisition settings. In order to reduce false detections due to brightness and contrast differences, radiometric normalisation is performed. One of the simplest approaches is to match first and second moments of image matrices (Ilsever and Ünsalan, 2012)

$$\tilde{\mathrm{I}}_2 = \frac{\sigma_1}{\sigma_2}\,(\mathrm{I}_2(x, y) - \mu_2) + \mu_1\ , \tag{5-8}$$

ensuring that global illuminance (statistically expressed in terms of μ) and contrast (variablity in terms of standard deviation σ) are equal for both images. While this approch is suitable for most orthophotos, it must be noted that local differences within an image cannot be compensated. These are caused by light and shade or by inproper configuration of image sensor and camera settings. In the case of OVC and OAC of the Multi Station Leica MS60, configuration options with regard to white balance and exposure time are limited, which is why adjacent textures may be captured with different settings. As a result, defect orthophotos with inhomogenous textures, as depicted in Figure 5-5a, may be obtained. Not only the visual representation, but also the difference image I_d is adversely affected, especially if such an image is subtracted from a homogeneous orthophoto

(cf. Figure 5-5b).

Artefacts of this kind can be prevented by either methodically modifying the photos before texturing or defining a constant white balance and exposure time for the data acquisition of an entire defect. Such configuration options are available via GeoCOM for image recordings with OVC and OAC.

(a) Orthophoto based on OVC textures with automatic white balance and exposure time selection

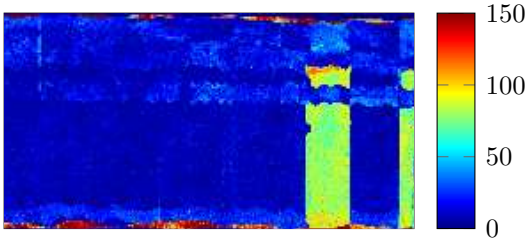

(b) Difference image of orthophotos with homogeneous and inhomogenous textures

Figure 5-5: Influence of inhomogenous textures on image differencing due to different white balance and exposure time settings

5.1.3 Identification of changes

The next step is to compute the difference image I_d from the geometrically aligned and radiometrically matched orthophotos. With slight relative misalignments of adjacent textures on the 3D photo model, intensity differences are determined for unchanged regions in the orthophotos as well (cf. Figure 5-6a). The magnitude of the intensity differences mainly depends on the inherent frequencies, i.e. on visual irregularities of the surface and on the image noise. Therefore, the difference image I_d is smoothed with a Gaussian kernel first, followed by thresholding with Otsu's method (cf. Chapter 4.1.1) for obtaining a binary image I_b, indicating pixels affected by change (cf. Figure 5-6b).

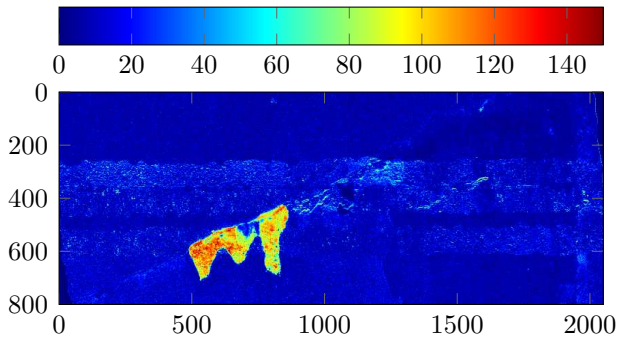

(a) Difference image I_d of preprocessed orthophotos

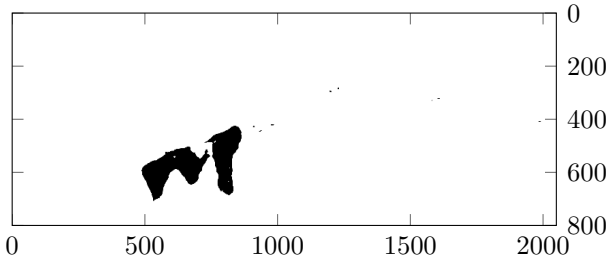

(b) Thresholded image I_b with Otsu's binarisation

Figure 5-6: Difference image I_d and binary image I_b as a result of change detection analysis

As shown in Figure 5-6b, the increasing efflorescence area (cf. Figure 5-2) can be reproduced well. The resulting segmentation image is subsequently analysed on coherent image regions, i.e. multiple changes are clustered and thus identified for an orthophoto pair. Analogous to defect detection (cf. Chapter 4.1.2), clustering is performed with the spatial connectivity based DBSCAN algorithm (cf. Figure 5-7a).

(a) Identified changes by applying DBSCAN algorithm to the segmented difference image I_b

(b) Identified changes by finding their contours in the binary image I_b

Figure 5-7: Identification of changes on a concrete dam with an orthophoto pair

An alternative to the approach of checking each pixel on spatial connectivity is to determine the outer boundary of connected pixel areas in I_b (cf. Figure 5-7b) with border following routines, as presented in Suzuki and Abe (1985). Although the algorithm is more than thirty years old, it is still very widespread and commonly implemented for finding contours in binary images, as e.g. the `findContours` module in OpenCV.

5.1.4 Image-based evaluation of surface conditions

Change detection analysis based on the pixelwise comparison of grayscale intensities has been proved viable with the above presented procedure. Due to spatial information provided by orthophotos, these changes can now be quantified for the first time. For instance, the extent of efflorescence around cracks and joint openings may be characterised in terms of thickness and area of coverage. Note that only the latter can be derived from images, however. Consider the polygon contour of the detected area affected by change in Figure 5-7b: its area may be computed using the shoelace formula (Braden, 1986)

$$A = \frac{1}{2}\left|\sum_{i=1}^{n-1} x_i\, y_{i+1} + x_n\, y_1 \sum_{i=1}^{n-1} x_{i+1}\, y_i - x_1\, y_n\right| , \tag{5-9}$$

where $(x_i,\, y_i)$ are coordinates of the polygon's vertices and n represents the number of its sides. The evaluation of the formula for the identified polygon in Figure 5-7b yields an area of $38\,650\,\mathrm{mm}^2$.

Quality assessment of image-based surface evaluation

It is apparent that the proposed approach gives unprecedented opportunities to evaluate the concrete surface of a dam without the requirement of direct access. At this point, the quality for such change indications is of interest. In order to assess the accuracy of quantification, changes on the dam's surface were simulated using objects whose precise area is known. For this specific purpose, an A4 sheet with a nominal area of 62 370 mm^2 (210 mm × 297 mm) was attached to the dam surface in the region of investigation. The results of the change detection analysis are visualized in Figure 5-8.

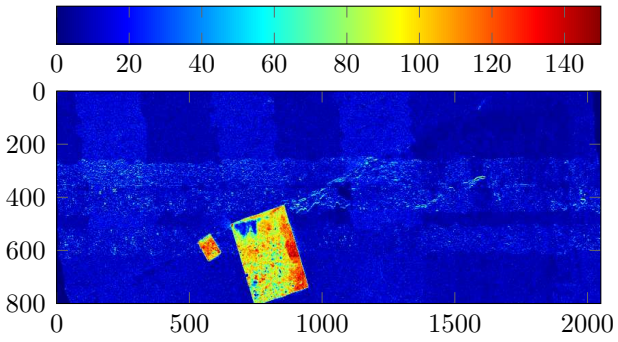

(a) Difference image I_d

(b) Orthophoto of the defect, overlayed with contours of identified changes (red contour)

Figure 5-8: Results of the pixel-based change detection analysis for a simulation with A4 sheet attached on concrete dam

Using Equation (5-9), the area of change, represented by the A4 sheet, was determined to be 62 789 mm^2, which corresponds to an overestimation compared to the nominal dimensions of $\Delta A = 419\,\text{mm}^2$. The origins of the uncertainty were investigated in an experiment, in which a similar test setup as for testing scanning precision (cf. Figure 3-14a) or the OAC misalignment (cf. Figure 3-29) has been established. The basic intention is to gather orthophotos of a scene with an A4 sheet attached on a building wall from different setup points and incident angles. Referred to an orthophoto depicting the scene without the sheet, changes are detected and quantified using the previously described procedure (see Figure 5-9). The deviations of computed and nominal area of an A4 sheet are outlined in Table 5-1.

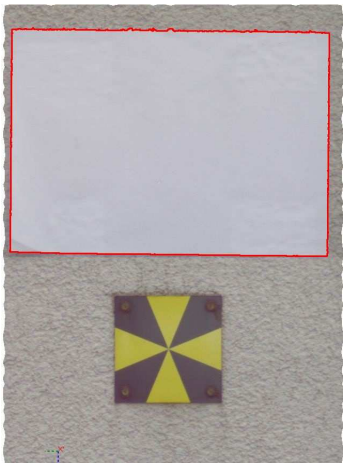

Figure 5-9: Orthophoto from P_2 overlayed with contours of the detected changes

Considering photos from different setup points, the detected areas of change differ with 70 mm^2 maximum, which corresponds to a total area difference of 0.1%. In fact, the quality of change quantification is less susceptible to the incident angle than to the object-to-instrument distance. The computed error in the aforementioned experiment is approximately two, three times larger, as is the distance to the concrete wall (51 m). The reason for the linear dependence is the effective pixel size, which increases linearly with the distance. With larger pixels, the changes or, more precisely, the contour lines of the regions of interest cannot be reproduced that well. The longer the contour line, i.e. the bigger the changing area, the larger is the resulting error. To correctly compare results, a new quantity ϵ is therefore introduced

$$\epsilon = \frac{\Delta \mathrm{A}}{p \cdot d} \left[\frac{\mathrm{mm}^2}{\mathrm{mm} \cdot \mathrm{mm}} \right] , \tag{5-10}$$

which considers the influencing parameters: the object-to-instrument distance d and the contour p of the detected region of interest. Inserting the parameters for the experiment at the concrete dam, a quality measure of $\epsilon = 8$ ppm was derived, which corresponds well with the values in Table 5-1.

Table 5-1: Quality evaluation of the change detection analysis in terms of nominal-actual area comparison of an A4 sheet for setup points with different incident angles

point	**incident angle [^{g}]**	**avg. distance [m]**	**area difference [mm^2]**	**ϵ[ppm]**
P_1	59	30.0	185	6
P_2	95	24.3	115	5
P_4	80	25.0	173	7

In other experiments comparing nominal-actual dimensions of an A4 sheet, $\epsilon \leq 10$ ppm was determined. To introduce a universal rule of thumb applying for all kind of objects, further investigations are required of course. Nonetheless, a comparative value and a rough estimate for the quality of the object detection with an IATS are obtained.

5.2 Object-based change detection analysis

In the past, two primary approaches were established for change detection analysis based on remote sensing data: the more traditional pixel-based (cf. Chapter 5.1) and the object-based method. While statistical computations are necessary for the pixel-oriented analysis, objects are extracted and its features are regarded in the latter approach. Rather than comparing pixel intensities, monitoring is provided by analysing the object's size,

shape and texture. Comparing these two methods, it has been shown that the object-based feature extraction promises advantages, especially for small structural changes (Niemeyer et al., 2007).

For the purpose of evaluating multitemporal orthophotos of a concrete dam, the principle idea is to consider defects as an elementary unit in the object space. Dependent on the type of defect, different methods for object extraction from images are applied. While the extent of efflorescence may be characterised as a polygon and segmented with techniques described in Chapter 5.1, cracks are better represented as polylines. Properties of a crack object could be length and width but their determination is unfeasible with the image processing techniques introduced so far. An alternative approach is presented in the following section, which enables the image-based delineation and monitoring of cracks.

5.2.1 Crack delineation and measurement with Poly-Fly-Fisher algorithm

In principle, the challenge is to delineate the crack as a polyline by identifying its characterising points from a digital image. Once the crack is sampled, the width is determined at those points. Therefore, the points need to be determined reliably, which is why a robust algorithm is prefered over a fully automated solution. Considering Figure 5-10, it becomes apparent that meeting both criteria is difficult. In fact, the task is referred to as ill-posed, as multiple possible pathes exist when considering the intensity values of an image matrix. As demonstrated in Dare et al. (2002), a minimal user interaction is sufficient to decrease the number of possibilites. Start and end point are e.g. required in the *route-finder* and the *poly-fly-fisher* algorithm. The latter algorithm's practicul use for crack width measurements has been demonstrated in the *Digitales Rissmess-System* (DRS) (Stratmann et al., 2008). The system evaluates close shots from a SLR camera with a cylindrical attachment, which has to be pressed against the concrete surface.

Figure 5-10: Exemplary orthophoto of a defect with ambiguous crack path

Crack delineation

A first but rather poor approximation of the crack path is obviously achieved by drawing a straight line between the two selected points. The result is subsequently refined with the poly-fly-fisher algorithm by gradually adding new points to the polyline. Beginning

at the start point, a series of 100 profiles is built up in the range of ±90° relative to the straight connection line (cf. Figure 5-11b). Along each profile, a considerable number of points with regular spacing are defined up to a predefined distance s (e.g. 11 px). Gray value intensities are computed with bilinear interpolation and summed up for a profile. The one with the largest intensity sum defines the direction for computing the next point at distance s. The procedure is repeated until the end point has been reached. Potential results for crack delineation in an orthophoto generated from data of a Leica MS60 (cf. Figure 5-11a) are depicted in Figure 5-11c.

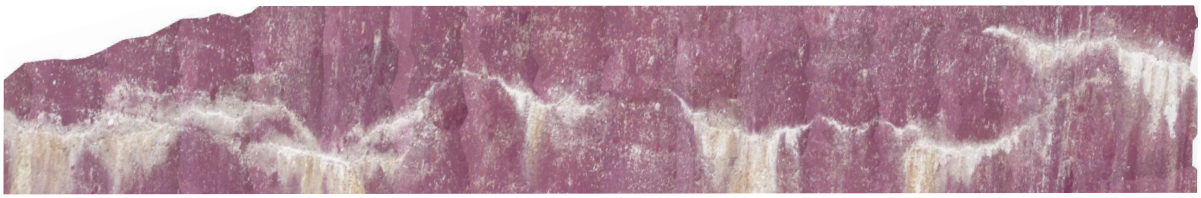

(a) Original orthophoto

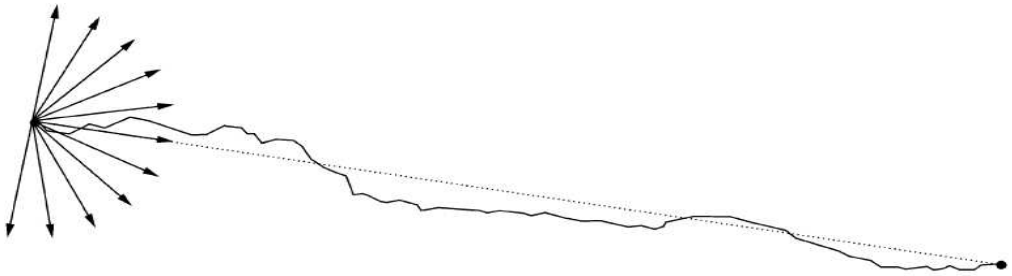

(b) Schematic figure of a crack and the profiles for delineation (Dare et al., 2002, p. 459)

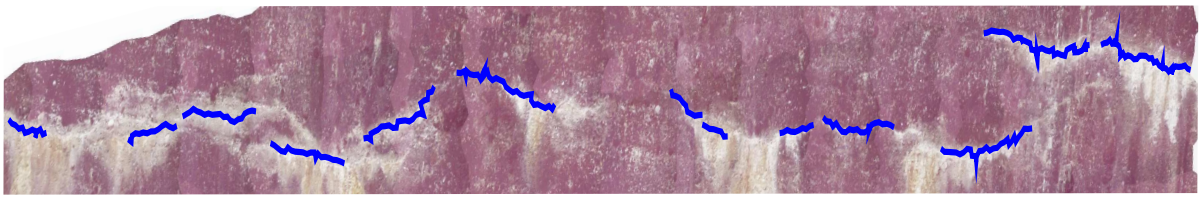

(c) Orthophoto overlayed with extracted crack polylines

Figure 5-11: Crack delineation with poly-fly-fisher algorithm

Crack width measurement

Based on the path of the crack, the width is eventually estimated. At the centre of each connection line between polyline points P_i and P_{i+1}, a perpendicular profile with 21 px, that is 10 px in both directions, is defined. In order to increase the accuracy, pixel intensities are interpolated at 210 points along the profile ($-10 \leq p \leq 10$). Considering the grayscale intensity function $f(p)$ along the profile, it is assumed that a drop-off in brightness indicates the transition line of the crack. Therefore, an adaptive threshold t is

computed according to the intensity function, so that

$$t = o - g \cdot (\max\{f(p)\} - \min\{f(p)\}) \ , \tag{5-11}$$

where o (offset) is defined as the intensity value of the central point lying on the connection line and g (gain) is set to 0.5 (Dare et al., 2002). The intensity function f for a profile is depicted in Figure 5-12a. Figure 5-12b shows a typical outcome of crack width measurements for a representative crack on a concrete dam.

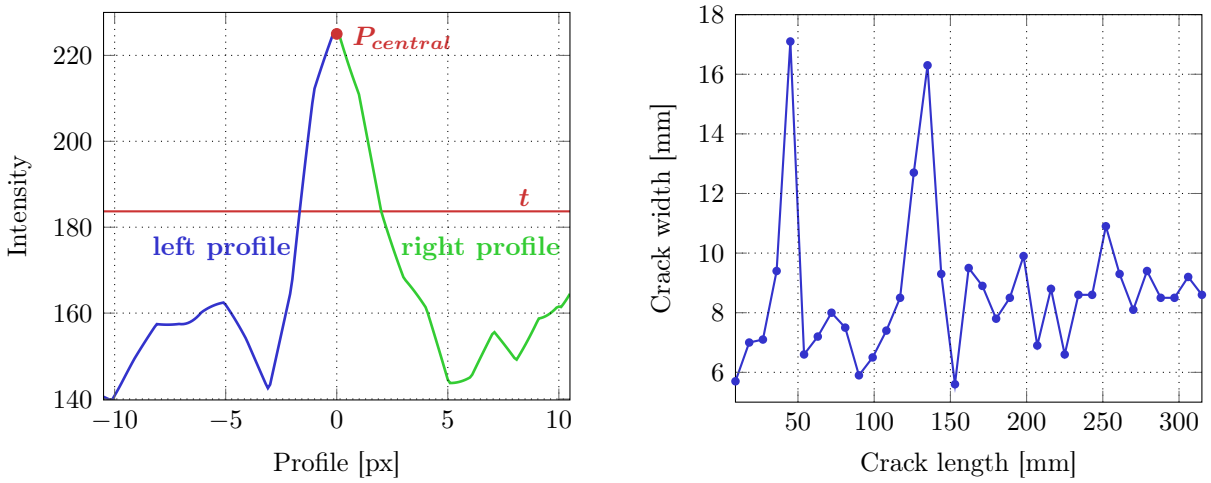

(a) Determination of crack width for one profile

(b) Computed width along delineated crack

Figure 5-12: Determination of the crack width with the poly-fly-fisher algorithm

5.3 Conclusion

Two different approaches for identifying changes on a surface were examined in the last sections. As demonstrated with practical investigations, both, the pixel-based and the object-based method, yield results with valuable information. As the crack delineation with the poly-fly-fisher is semiautomatic, the proposed pixel-based method is preferably used (cf. Chapter 5.1). Moreover, it is considered as an area-based technique and is thus applicable for all kind of defects. Based on the insights gained in this thesis, the following procedure (see also Figure 5-1) is proposed:

1. Pre-processing:

   (a) Radiometric normalisation: Global illumination differences between two digital images are eliminated by matching their first and second order moments. Nonetheless, the orthophotos must be homogeneous in brightness and contrast, i.e. adjacent textures must have similar image properties.

   (b) Image alignment: An exact pixelwise overlap can be achieved by aligning the orthophotos. The transformation parameters for the affine transformation are computed based on corresponding points, found in both images. To detect and descript features in an image, the SIFT operator is used.

2. Image differencing & Thresholding: In order to reduce noise in the difference image, Gaussian smoothing is applied. With Otsu's binarisation method, an ideal threshold according to the apparent difference image properties is computed.

3. Clustering: The segmented pixels are clustered with the DBSCAN algorithm. Spatially unconnected pixels are classified as noise.

4. Evaluation of changes: The clustered and segmented pixels represent the identified changes. Due to the additional information of the orthophotos, the surface changes are evaluated in terms of true area differences (e.g. mm^2).

Using reference objects for simulating changes, investigations have been performed on the quality of change detection and evaluation. It has been found that the influence of the incident angle of acquisition is insignificant. Crucial for the quality are the object-to-instrument distance and the contour length of the region of change. When considering these parameters, a universal value of $\epsilon \leq 10\,\text{ppm}$ for the newly introduced quality measure is achieved with the proposed method.

6 Significance of the proposed surface monitoring solution

With increasing operating life of water dams, continous monitoring of the dam's behaviour becomes more and more important. As there are no sensors with the capability to assess and monitor the concrete's state, visual inspections have to take place at regular intervals. Apart from daily inspections by the operating staff, the surface's current state has to be documented every few years according to national regulations. The competent surveyors carry out and submit the documentation to the public authorities. An example of such a documentation for the Drossen dam (Kaprun, Salzburg) is given in Figure 6-1. A typical photo for documenting the dam's surface is shown on the left and on the right side the corresponding CAD drawing of the Drossen dam with its defects is depicted (cf. Chapter C for the complete plan).

(a) Photograph of the downstream side of the dam (Verbund, 2011, p. 13)

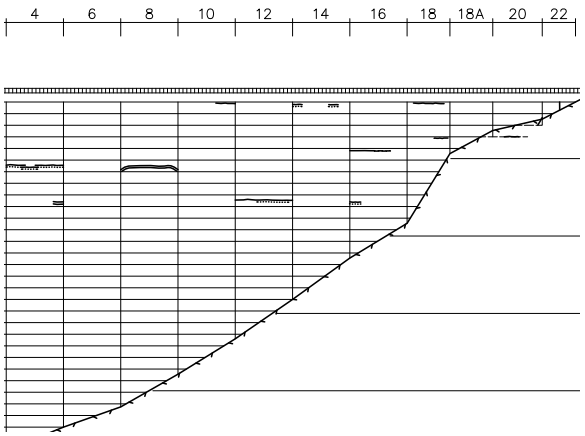

(b) CAD drawing showing defect locations (Verbund, 2011, p. 11)

Figure 6-1: Traditional approach for surface documentation of the righ-thand side of the Drossen dam

This traditionally used method revealed insufficiencies, which is why various new and alternative approaches have been tested in the past. In this thesis the major components of a surface monitoring solution with an IATS are presented. Compared to the traditional approach, not only texture but also geometry content is acquired and both types of data are merged to obtain a digital 3D photo model of the dam. Figure 6-2 shows such a surface model for the right-hand side of the Drossen dam (same surface as displayed in Figure 6-1), where overview and high resolution images are used in combination. Consequently, photos can be rectified and thus measurements can be performed on the dam's concrete surface without the need of direct access. In particular, automatically identified defects can be analysed, which opens up unprecedented opportunities for the dam safety assess-

ment. For instance, HR orthophotos such as Figure 6-3 (defect in block 16 of the Drossen dam, see also Figures 6-1b and 6-2) provide valuable data for future surveys to identify and quantify surface changes. It is therefore considered as improvement to the currently used methodology for surface documentation and evaluation and shall not replace other geodetic or geotechnical measurements.

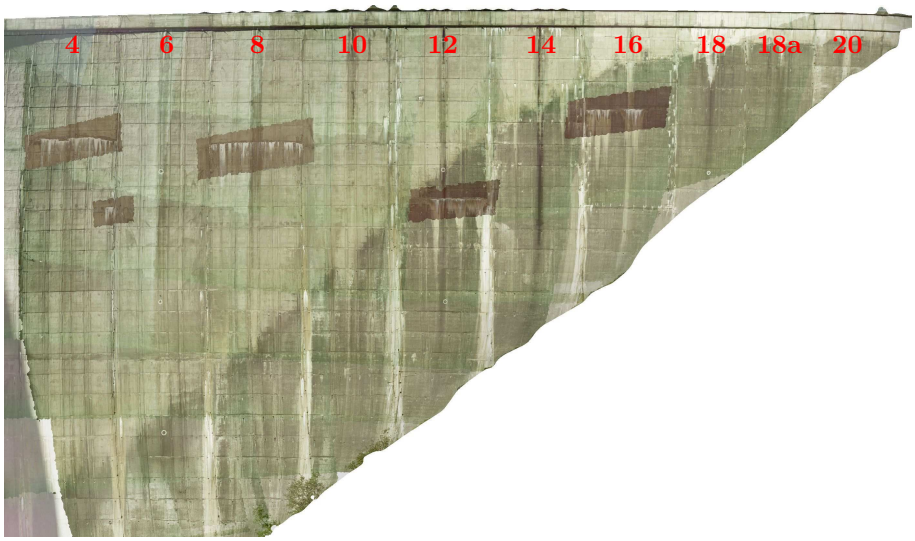

Figure 6-2: Orthophoto of a 3D photo model of the right-hand side of the Drossen dam, 5 cm/px

Figure 6-3: Rectified detail image of the defect in block 16 of the Drossen dam, 2 mm/px

The major goal is to contribute to the comprehensive dam monitoring system and thus to provide reliable, valuable data for civil engineers and public authorities for dam safety assessment. From the perspective of the competent surveyor, the IATS is operated like a standard total station. Hence, it is easy to use and a lot of steps are automated as well. Concerning data acquisition and evaluation, approximately one to two working days are required. In particular, scanning with a state-of-the-art total station is the most time-consuming part. In the case of the Drossen dam, it took about 5 hours to acquire the point cloud data of the entire dam (1000 Hz scan rate for an average grid of 10 cm×10 cm). However, as long as the dam's geometry is not changing significantly due to ambient conditions (may cause image distortions), the same digital surface model can be used for texturing and hence a lot of time can be saved (no specific threshold is defined).

A comparison of the key features of the traditional and the proposed approach for surface documentation is given in Table 6-1.

Table 6-1: Key characteristics of the traditional and the proposed approach for surface documentation

Traditional approach	**Proposed approach**
Simple approach requiring a standard SLR camera only.	Easy to use for surveyors, as no special expertise is necessary (cf. surface mapping with an inspection drone).
The key components of the documentation are photos and a CAD drawing of the dam.	An overcast sky is perfect for data acquisition. Scanning is adversely affected by rain and moisture, as well is direct sunlight likely to cause oversatured images (cf. Figure 3-30).
The outcomes are registered in a text document. It is stored for internal use and sent to public authorites every few years according to national regulations.	HR images of defects are captured either fully automatic with the IATS connected to a laptop or by operating its on-board software.
The task is commonly performed by surveyors.	The resulting 3D photo model provides information about size, shape and position of the texture content.
Photos captured with a SLR serve as a rough documentation only. Based on photos of defects, size, position or changes are almost impossible to derive.	Due to the magnification of the telescope, a spatial resolution of 0.9 mm is achieved at an object-to-instrument distance of 100 m. Hence, based on rectified images, highly accurate measurements can be performed directly on the concrete surface.
For closer examination, direct access to the region of interest on the dam's surface is required.	The system enables the registration of surface changes. Newly occured defects are automatically detected and structural changes of exisiting defects are identified and quantified.
There is a risk of missing out small defects. If they are not identified on-site, they will remain undiscovered, as the photo documentary cannot be used for image-based analysis.	

7 Conclusion

Concrete dams are critical structures, and thus their response to the enourmous acting forces is surveyed with an artificial neural network of sensors. Up to now, the long-term degradation process of concrete on the downstream and upstream side of the dam is assessed by visually comparing photographs of different epochs, captured from accessible points of view. As the currently used methodology reveals insufficiencies, a new approach for surface documentation and evaluation of large water dams is introduced in this thesis.

The principle idea is to acquire scan and image data from the dam's surface with a state-of-the-art total station. Geometry and texture information is first processed seperately and eventually merged together to obtain 3D photo models and orthophotos of the concrete surface. The geometrical quality of the reconstructed digital continous surface model from scattered point cloud data depends on numerous parameters, but has been revealed to be considerably good for the given circumstances. Investigations have shown average deviations of $\pm 5\,\mathrm{mm}$ of two surface models, generated from scan data of the Hierzmann dam at two different epochs. Texture mapping with oriented images provides a photorealistic 3D model with an adjacent texture accuracy at sub-pixel level (for OVC and OAC images). However, a drawback of using image content from an IATS is that photo settings are limited, thus making this approach highly susceptible to the ambient light conditions.

With orthophotos and 3D photo models, unprecedented opportunities arise to evaluate the concrete's condition of a water dam without the need of direct access. In this thesis, a novel surface monitoring solution is proposed, where concrete deficiencies are automatically identified on-site by running image processing techniques in real-time on a laptop connected to the IATS. Investigations have shown that reliable detections are achieved. In fact, the algorithm tends to mistakenly classify image content as critical, rather than missing out any defects. Results from prior surveys may help, but semi-automatic operation is suggested, especially if the system is used once every few years (i.e. not as a permanent monitoring solution). For every defect identified on-site, HR scans and images, coordinates and metadata are recorded to establish a defect database with characterising values and detailed orthophotos for each epoch.

Any visual changes on the concrete surface may indicate a potential threat to the structural integrity of the dam. Therefore, it is of great importance to closely monitor the defect situation, i.e. identify new defects and quantify changes of existing ones. An algorithm for automatic pixel-based change detection analysis in orthophotos was developed, which proved invariant to different light conditions, scale and image transformations. Area changes were simulated and determined with high accuracy. A new quality measure considering the object-to-instrument distance and the extent of changes is introduced.

References

3DReshaper (2016): (Version 11.0.9.23620), July 7th, 2016. Retrived from `http://www.3dreshaper.com/`.

Bajaj Chandrajit L., Bernardini Fausto, Xu Guoliang (1995): Automatic Reconstruction of Surfaces and Scalar Fields from 3D Scans. Proceedings of the 22Nd Annual Conference on Computer Graphics and Interactive Techniques. New York, NY, USA. pp. 109–118.

Berger Matthew, Tagliasacchi Andrea, Seversky Lee M., Alliez Pierre, Levine Joshua A., Sharf Andrei, Silva Claudio T. (2014): State of the Art in Surface Reconstruction from Point Clouds. Eurographics 2014 - State of the Art Reports. The Eurographics Association. p. 28.

Biedermann Rudolf (1980): Außerordentliches Verhalten der Staumauer Zeuzier. Wasser, Energie, Luft - Eau, énergie, air. 72(7/8). Baden. pp. 182–184.

Boissonnat Jean-Daniel (1984): Geometric Structures for Three-dimensional Shape Representation. ACM Trans. Graph. 3(4). pp. 266–286.

Braden Bart (1986): The Surveyor's Area Formula. The College Mathematics Journal. 17(4). pp. 326–337.

Bradski Gary, Kaehler Adrian (2008): Learning Opencv. O'Reilly Media, Inc. p. 555.

Camp Géraldine, Carreaud Pierre, Lançon Hervé (2013): Large Structures: Which Solutions for Health Monitoring? International Archives of the Photogrammetry, Remote Sensing and Spatial Information Sciences. XL-5(W2). XXIV International CIPA Symposium, Strasbourg, France. pp. 137–141.

Canny John (1986): A computational approach to edge detection. IEEE Transactions on Pattern Analysis and Machine Intelligence. PAMI-8(6). pp. 679–698.

Carr J. C., Beatson R. K., Cherrie J. B., Mitchell T. J., Fright W. R., McCallum B. C., Evans T. R. (2001): Reconstruction and Representation of 3D Objects with Radial Basis Functions. Proceedings of the 28th Annual Conference on Computer Graphics and Interactive Techniques. New York, NY, USA. pp. 67–76.

Cazals Frédéric, Giesen Joachim (2004): Delaunay Triangulation Based Surface Reconstruction: Ideas and Algorithms. Technical Report RR-5393, Project Geometrica, INRIA Sophia and Departement Informatik, ETH Zürich, Switzerland. p. 42.

Cheng Z.-Q., Wang Y.-Z., Li B., Xu K., Dang G., Jin S.-Y. (2008): A Survey of Methods for Moving Least Squares Surfaces. Proceedings of the Fifth Eurographics / IEEE VGTC Conference on Point-Based Graphics. Eurographics Association, Aire-la-Ville, Switzerland. pp. 9–23.

CloudCompare (2016): (Version 2.7) [GPL software]. Retrived from http://www.cloudcompare.org/.

Dare Paul, Hanley Harry, Fraser Clive, Riedel Björn, Niemeier Wolfgang (2002): An operational application of automatic feature extraction: The measurement of cracks in concrete structures. The Photogrammetric Record. 17(99). pp. 453–464.

DePalma Anthony (March 2008): Defects Go Unfixed for Years in Dozens of Dams, New York Comptroller Finds. The New York Times. Available at http://www.nytimes.com/2008/03/26/nyregion/26dams.html?_r=0.

Ehrhart Matthias, Lienhart Werner (2015): Image-based dynamic deformation monitoring of civil engineering structures from long ranges. Image Processing: Machine Vision Applications VIII. SPIE 9405. pp. CD-14.

Ester Martin, Kriegel Hans-Peter, Sander Jörg, Xu Xiaowei (1996): A density-based algorithm for discovering clusters in large spatial databases with noise. KDD-96. Spatial, Text & Multimedia. pp. 226–231.

Fröhlich Christofer, Mettenleiter Markus (2004): Terrestrial laser scanning - new perspectives in 3d surveying. International archives of photogrammetry, remote sensing and spatial information sciences. 36(Part 8). pp. 7–13.

Gomes Abel, Voiculescu Irina, Jorge Joaquim, Wyvill Brian, Galbraith Callum (2009): Implicit Curves and Surfaces: Mathematics, Data Structures and Algorithms. Springer Publishing Company, Incorporated. p. 317.

Gotsman Craig, Kazhdan Michael (2008): Poisson Mesh Reconstruction. Digital Geometry Processing, 2008. Available at http://www.cs.technion.ac.il/~cs236329/lectures/poisson_reconstruction.pdf.

Gotsman Craig, Keren Daniel (1998): Tight Fitting of convex Polyhedral Shapes. International Journal of Shape Modeling. 04(03n04). pp. 111–126.

Grimm David Eugen, Zogg Hans-Martin (2013): Leica Nova MS50. White Paper, Leica Geosystems AG, Heerbrugg, Switzerland. p. 12.

Hanusch Thomas (2010): Texture Mapping and True Orthophoto Generation of 3D Objects. PhD thesis, ETH Zürich, Switzerland. p. 140.

Hoppe Hugues, DeRose Tony, Duchamp Tom, McDonald John, Stuetzle Werner (1992): Surface Reconstruction from Unorganized Points. SIGGRAPH Comput. Graph. 26(2). New York, NY, USA. pp. 71–78.

Hughes John F., Dam Andriesvan, McGuire Morgan, Sklar David F., Foley James D., Feiner Steven K., Akeley Kurt (2013): Computer graphics: principles and practice (3rd ed.). Addison-Wesley Professional. p. 1264.

ICOLD (2013): Dam Surveillance Guide. Technical Report 158, International Commission on Large Dams. p. 109.

Ilsever Murat, Ünsalan Cem (2012): Two-Dimensional Change Detection Methods - Remote Sensing Applications. Springer. p. 72.

Kazhdan Michael, Bolitho Matthew, Hoppe Hugues (2006): Poisson Surface Reconstruction. Proceedings of the Fourth Eurographics Symposium on Geometry Processing. Eurographics Association, Aire-la-Ville, Switzerland. pp. 61–70.

Kuo Chuan-Chu, Yau Hong-Tzong (2005): A delaunay-based region-growing approach to surface reconstruction from unorganized points. Computer-Aided Design. 37(8). pp. 825–835.

Leica (2014): Leica Nova MS50 GeoCOM Reference Manual. Leica Geosystems, Heerbrugg, Switzerland. Version 5.50. p. 289.

Leica (2015): Leica MS60/TS60, User Manual. Leica Geosystems, Heerbrugg, Switzerland. p. 90.

Lipman Yaron, Cohen-Or Daniel, Levin David, Tal-Ezer Hillel (2007): Parameterization-free Projection for Geometry Reconstruction. ACM Trans. Graph. 26(3). New York, NY, USA.

Lowe David G. (2004): Distinctive image features from scale-invariant keypoints. International Journal of Computer Vision. 60. pp. 91–110.

Lucas Bruce D., Kanade Takeo (1981): An iterative image registration technique with an application to stereo vision. Proceedings of the 7th International Joint Conference on Artificial Intelligence - Volume 2. San Francisco, CA, USA. pp. 674–679.

Maar Hannes, Zogg Hans-Martin (2014): WFD - Wave Form Digitizer Technology. White Paper, Leica Geosystems AG, Heerbrugg, Switzerland. p. 12.

Maur Pavel (2002): Delaunay Triangulation in 3D. Technical Report DCSE/TR-2002-02, University of West Bohemia in Pilsen, Departement of Computer Science and Engineering. p. 53.

Mencl R., Müller H. (1997): Interpolation and Approximation of Surfaces from Three-Dimensional Scattered Data Points. Scientific Visualization Conference (dagstuhl '97). pp. 223–232.

Micron (2006): MT9P031 Image Sensor Product Brief. Micron Technology, Inc., Boise, ID, USA, 2 edition. Datasheet.

Mullen Patrick, De Goes Fernando, Desbrun Mathieu, Cohen-Steiner David, Alliez Pierre (2010): Signing the Unsigned: Robust Surface Reconstruction from Raw Pointsets. Computer Graphics Forum. 29(5). pp. 1733–1741.

Niemeyer Irmgard, Marpu Prashanth Reddy, Nussbaum Sven (2007): Change detection using the object features. 2007 IEEE International Geoscience and Remote Sensing Symposium. pp. 2374–2377.

Ohio Department of Natural Resources (1999): Dam safety: Problems with concrete materials. Technical report, Division of Water Fact Sheet.

Otsu Noboyuki (1979): A Threshold Selection Method from Gray-Level Histograms. IEEE Transactions on Systems, Man, and Cybernetics. SMC-9(1). pp. 62–66.

Psarakis Emmanouil Z., Evangelidis Georgios D. (2008): Parametric Image Alignment Using Enhanced Correlation Coefficient Maximization. IEEE Transactions on Pattern Analysis & Machine Intelligence. 30(10). pp. 1858–1865.

Regan Patrick J. (2010): Dams & Civil Structures: An Examination of Dam Failures vs. Age of Dams. Hydro Review.

Remondino Fabio (2003): From point cloud to surface: the modeling and visualization problem. International Archives of the Photogrammetry, Remote Sensing and Spatial Information Sciences. XXXIV(5/W10). p. 11.

senseFly (2016): Documenting a large dam with senseFly's albris inspection drone. Available at `https://www.sensefly.com/fileadmin/user_upload/sensefly/user-cases/2016/senseFly-Case-Study-Tseuzier-Dam.pdf`. Case study.

Sotoodeh S. (2007): Hierarchical clustered outlier detection in laser scanner point clouds. The international archives of the photogrammetry, remote sensing and spatial information sciences. 36(3/W52). pp. 383–388.

Stratmann Rafael, Birtel Veit, Mark Peter, Neuß Helmut, Niemeier Wolfgang, Riedel Björn, Ziem Eberhard (2008): Digitale Erfassung und Bewertung von Rissen. Beton und Stahlbau. 103(4). pp. 252–261.

Suzuki Satoshi, Abe Keiichi (1985): Topological structural analysis of digitized binary images by border following. Computer Vision, Graphics, and Image Processing. 30(1). pp. 32–46.

Topcon (2007): TopSURV OnBoard for IS, Scanning, Reference Manual. Topcon Corporation, Tokyo, Japan. p. 31.

Topcon (2016): IS-3 Imaging Station. Topcon Corporation. Brochure.

Trimble (2015): Trimble S9 and S9 HP Total Station. Trimble Navigation Limited, Westmoor Dr, USA. Datasheet.

Verbund (2011): Rissaufnahme der luftseitigen Maueroberfächen. Technical report, Kraftwerk Kaprun - Oberstufe. p. 16.

Weyrich T., Pauly M., Keiser R., Heinzle S., Scandella S., Gross M. (2004): Post-processing of Scanned 3d Surface Data. Proceedings of the First Eurographics Conference on Point-Based Graphics. Aire-la-Ville, Switzerland. pp. 85–94.

A Camera model parameters in the LandXML file

For each image captured with the on-board software of e.g. Leica MS50 (Viva) or MS60 (Captivate) Multi Station, a record is stored to the LandXML file. The XML tag `TPSImage` contains image dimensions and orientation parameters of the telescope, i.e. Hz, V angle and inclination values. Additionally, the projection centre of the camera is provided (cf. Figure A-1a), considering telescope orientation, station coordinates and camera type (OVC or OAC).

```
<TPSImage uniqueID="561_2" InteriorOrient="3_2" CameraCalib="2_2" ChipWindow="1_2"
    horizAngle="168.018724250459510" zenithAngle="129.602300000675570"
    InclinationLength="-0.000609693397965" InclinationCross="0.005090622226627" Width=
    "2560" Height="1920" Dimension="Landscape">
<landxml:DocFileRef name="Img_Pano_04_11_110516_184620" location="MA_SK_1105_xml"
    fileFormat="jpg"/>
<ExteriorOrientation ProjectionCenterX="41.577590" ProjectionCenterY="81.091622"
    ProjectionCenterZ="-29.831197" Phi="168.018724250459510" Theta="
    129.602300000675570" Kappa="0.000000000000000"/>
</TPSImage>
```

Every image, whether acquired with OVC or OAC, is referenced to the interior orientation block at the end of the file (see below). Camera calibration parameters, which are determined during production, are listed under the tag `CameraInfo` at the end as well. It contains camera misalignment parameters in terms of tilt ω (combination of φ, ϑ, κ, cf. Figure A-1b) and offset $\vec{o}$ w.r.t. the telescope (cf. Figure A-1a). The units of the LandXML attributes required for texture mapping are listed in Table A-1.

```
<CameraInfo uniqueID="2_2" CameraType="OVC" CameraModel="Micron MT9P031" PixelSize="
    2.200000E-006" PixelScale="1" ChipDimensionWidth="0" ChipDimensionHeight="0"
    ProjectionCenterX="0.016082" ProjectionCenterY="0.060565" ProjectionCenterZ="
    0.054600" Phi="-0.184948082915038" Theta="0.077871240406377" Kappa="
    0.172810027554797" DistortionK1="0" DistortionK2="0" ChipWindow="1"/>
<InteriorOrientation uniqueID="3_2" PrincipalPntX="1307.53" PrincipalPntY="948.408"
    CameraConstant="2.084844E-002" CrossHairPosX="0" CrossHairPosY="0"
    VirtualCameraConstant="0"/>
<ChipWindow uniqueID="1_2" Xposition="0" Yposition="0" ChipWindowWidth="2560"
    ChipWindowHeight="1920"/>
```

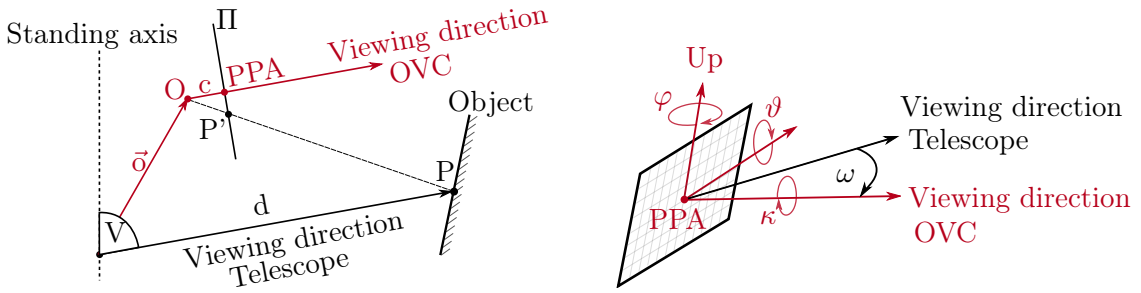

(a) Cross-sectional illustration of the camera position and the orientation

(b) Tilt of the camera viewing direction w.r.t. to the optical axis of the telescope

Figure A-1: Illustration of the interior orientation parameters for the OVC

Table A-1: Units of the LandXML attributes associated with imaging

XML tag	Parameter	Unit
`TPSImage`	horizAngle, zenithAngle	gradians
	InclinationLength InclinationCross	pixels
	Width, Height	pixels
`ExteriorOrientation`	ProjectionCenterX ProjectionCenterY ProjectionCenterZ	meters
	Phi, Theta, Kappa	gradians
`InteriorOrientation`	PrincipalPntX PrincipalPntY	pixels
	CameraConstant	meters
	CrossHairPosX CrossHairPosY	pixels
`ChipWindow`	Xposition, Yposition	pixels
	ChipDimensionWidth ChipDimensionHeight	pixels

B Software proposal for in-situ defect management

Figure B-1 depicts the developed GUI, which was used for on-site identification and registration of defects. The GUI consists of two major parts: the image frame and the control panel. OVC images are depicted and overlayed with the image processing results. A slider offers the user the opportunitiy to switch between all OVC images acquired in the course of the survey. The control panel contains switches for the variable defect detection parameters, as well as controls for interacting with the SQLite database, which contains information from the last surveys (cf. Figure B-2).

Figure B-1: GUI for identifying and registering defects

	Id	Hz1	V1	Hz2	V2	MeasureMask	Station
1	1	139.29349	114.92124	140.58331	115.17652	1	1
2	2	140.67064	108.03546	141.45663	108.3512	1	1
3	3	131.85013	115.94907	133.37508	116.59398	1	1
4	4	149.32427	115.57158	158.85016	117.08309	1	1
5	5	142.30413	115.34317	147.32907	115.91548	1	1
6	6	150.66112	117.3854	151.48069	118.2923	0	1
7	7	165.02457	112.15854	167.08023	113.57601	1	1
8	8	167.08023	108.67199	169.13589	109.3908	1	1
9	9	161.57161	108.65855	163.13014	109.90135	1	1
10	10	158.56874	108.19502	159.58985	109.31018	0	1
11	11	167.26161	112.13167	169.25009	114.86583	1	1
12	12	156.21677	108.49061	157.39311	109.19636	0	1
13	13	152.06587	108.47717	152.89217	108.84665	0	1
14	14	153.44303	108.47717	154.18871	108.83994	0	1
15	15	165.05145	109.91479	167.08695	110.97621	1	1
16	16	139.58273	127.3431	143.72763	130.52063	1	1
17	17	136.47237	121.3172	138.17198	122.45923	1	1
18	18	133.98005	126.20107	135.33034	127.10126	1	1

Figure B-2: Table of local detection results in defect database

Switches for the variable detection parameters are arranged in the lower left corner of the GUI. The user has the choice whether edge detection or thresholding according to pixel intensities should be applied to the photo for segmentation.

In the central part of the control panel, a drop-down menu is implemented. It is intended to switch between two essential modes for defect management:

1. Analyse mode: All computations described in Chapter 4.1 are performed for every image separately and before depiction in the image frame. In principle, this mode is established for adjusting the parameters and thus for the operator to see how they affect the defect detections. In this mode, the button "Compute all" is set active and when pressed, detections are computed from single images and combined to get a consistent set of defects, which are subsequently stored in the database.

2. Presentation mode: All MBRs of detected defects, which are read in from the database, are displayed, whereas individual pixel clusters are not depicted in this mode anymore. Mistakenly identified vegetation, for instance, can be removed at this point. By selecting the appropriate MBR and pressing the "Mask Selected" button, the measure mask in the defect database is set to zero and hence this entry will be ignored in the course of the data acquisition of defects.

Detected defects are initially stored in a temporary table in the SQLite database in terms of Hz and V angles. This table is valid, as long as the acquisition point corresponds to the current station (i.e. as long as deviations are less than 5 cm). Entries marked with the appropriate measure mask are registered by pressing the "Acquire HR data" button in terms of HR scan, image data and coordinates. These coordinates are stored in a permanent table in the database and used as additional information for all future surveys from arbitrary setup points.

C Traditional plan of a water dam showing defect locations

A traditional CAD drawing of the Drossen dam is presented on the next page (Verbund, 2011, p. 11)). It provides a rough overview of position and extent of the defects on the concrete dam.

Kraftwerk Kaprun Oberstufe
Drossensperre

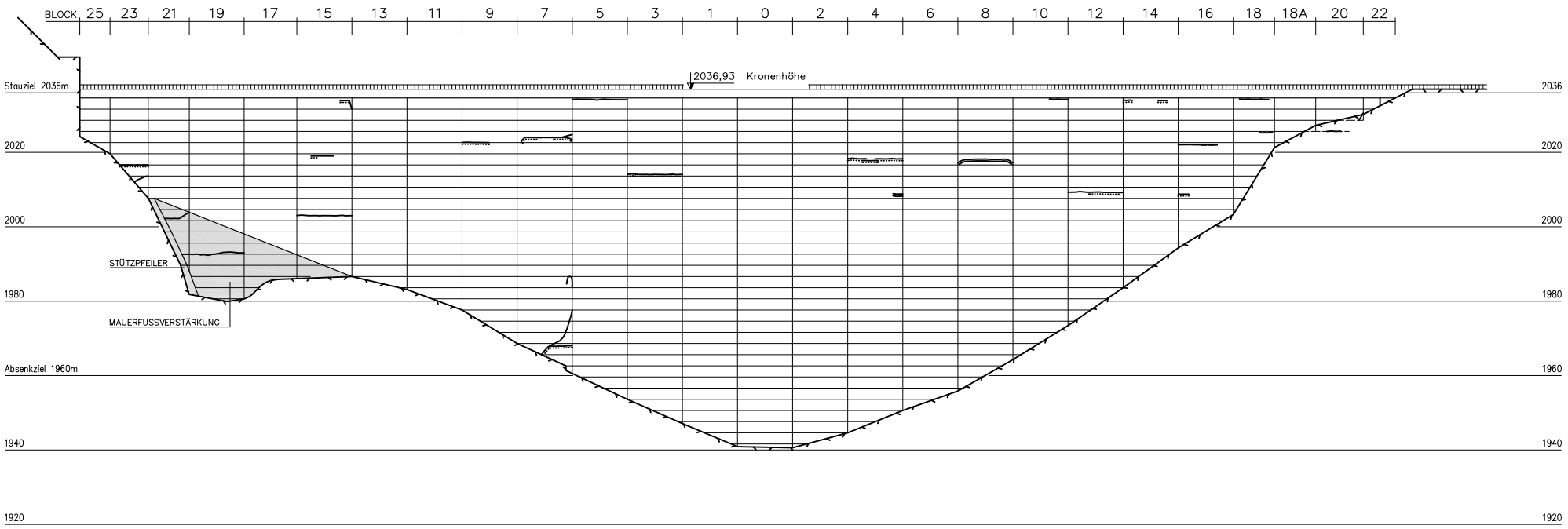

Legende

Riss

Riss feucht / versintert

Rissaufnahme der luftseitigen Mauerfläche

Maßstab:	Aufnahmedatum:	Plan Nr. :	Version
1:1000	14.9.2011	KO–Y 213.1	03